https://doi.org/10.5194/egusphere-2026-3331
Preprint. Discussion started: 25 June 2026

Ensemble reconstruction of the Greenland Ice Sheet evolution through the last deglaciation

Lucía Gutiérrez-González[1,2], Ilaria Tabone[3], Alexander Robinson[4], Jorge Álvarez-Solas[2], Jan Swierczek-Jereczek[1,2], Britta Grusdt[4], and Marisa Montoya[1,2]

[1]Department of Earth Physics and Astrophysics, Complutense University of Madrid, Madrid, Spain.
[2]Geosciences Institute, CSIC-UCM, Madrid, Spain.
[3]Department of Geophysics, University of Concepción, Concepción, Chile.
[4]Alfred Wegener Institute, Helmholtz Centre for Polar and Marine Research, Potsdam, Germany.

Correspondence: Lucía Gutiérrez-González (lucgut03@ucm.es)

Abstract. The last deglaciation offers valuable insights into ice-climate interactions, as extensive paleoclimatic records document the retreat of ice sheets through a period of major climate changes. During this interval, the Greenland Ice Sheet (GrIS) retreated from its extensive Last Glacial Maximum (LGM) configuration to its present state, passing through the Holocene Thermal Maximum (HTM), when temperatures exceeded present-day values. Despite the large amount of paleoclimatic data available, ice-sheet models struggle to reproduce key aspects of the observational record, and the magnitude of the GrIS contribution to sea level throughout this period, in particular during the LGM and the HTM, remains highly uncertain. In this study, we evaluate an ensemble of 3,000 simulations of the GrIS performed with the Yelmo ice-sheet model against different observational constraints. These include: (1) the LGM ice-sheet extent, (2) ice-core-derived surface elevations, (3) an ice-extent retreat chronology based on the recent PaleoGrIS dataset, and (4) the present-day ice-sheet configuration (ice thickness, ice cover, ice-surface velocity, and bedrock elevation). We characterize the impact of the parameters perturbed along the ensemble on the GrIS evolution using an emulator based on the XGBoost algorithm combined with the SHAP (SHapley Additive exPlanations) framework. This analysis reveals that the climatic parameters (surface melting corrections and ocean thermal sensitivity) dominate the impact. By identifying the simulation that best matches these observables, we provide a constrained reconstruction of the GrIS during the last deglaciation that substantially improves upon previous reconstructions. We obtain a GrIS contribution to global sea level with respect to present of $-5.75\,\mathrm{m}$ of sea-level equivalent (SLE) at the LGM (with an uncertainty range of -3.93 to -6.31 m) and +0.45 m after the HTM warming (with an uncertainty range of 0.43 to 1.18 m). This is in the upper range of previously existing estimates, indicating a comparatively mid-to-high GrIS sensitivity to climate changes over the last deglaciation.

1 Introduction

Understanding and accurately modeling the mechanisms driving major ice-sheet transformations has become increasingly important given contemporary global warming trends, as accelerated ice-sheet melting poses severe threats to coastal communities and marine ecosystems worldwide (IPCC, 2021; Kulp and Strauss, 2019). To this end, the last deglaciation constitutes a unique

https://doi.org/10.5194/egusphere-2026-3331
Preprint. Discussion started: 25 June 2026

period for advancing our understanding of ice-climate interactions, as extensive paleoclimatic records document the retreat of the ice sheets during a period of substantial climate transitions.

During the Last Glacial Maximum (LGM), around 21 kyr ago, surface temperatures over Greenland were approximately 20°C below present-day values (Kindler et al., 2014). Nevertheless, the Greenland Ice Sheet (GrIS) reached its maximum extent between 19 and 17 kyr ago, during what we refer to as the local LGM (Leger et al., 2025; Funder et al., 2011). Its maximum grounded area in this period is between 2.8 and 3.1 million km^2, with estimates of its contribution to global sea level reduction ranging widely from 2.6 to 7.5 m sea-level equivalent (SLE) relative to the present day (Buizert et al., 2018; Lecavalier et al., 2014; Tabone et al., 2018; Bradley et al., 2018; Gutiérrez-González et al., 2026a; Leger et al., 2025; Lauritzen et al., 2024). These estimates imply that the GrIS was between 35 and 100% larger in volume than it is today, reflecting both the scale of past change and the substantial uncertainties involved.

The subsequent deglaciation, which began around 17-16 kyr ago, was characterized by rapid and heterogeneous retreat during the Bølling-Allerød warming (16-14 kyr ago), with mass loss rates sometimes exceeding current levels by 2 to 7 times (Vasskog et al., 2015). Despite limited regional readvances during the Younger Dryas and early Holocene cold spells, the GrIS continued to shrink, reaching its minimum extent between 5 and 3 kyr ago, following the Holocene Thermal Maximum (HTM, Young and Briner, 2015). This period, which we define here as spanning 10–6 kyr ago (Buizert et al., 2018), is of particular relevance as summer temperatures over Greenland are estimated to have been approximately 3°C above modern values (Buizert et al., 2018; Briner et al., 2016), with some melt-based reconstructions suggesting anomalies exceeding 5°C (Lecavalier et al., 2017). This makes the HTM a suitable period for understanding the response of the ice sheet to sustained warming. The GrIS subsequently readvanced to its present-day configuration (Vasskog et al., 2015; Yang et al., 2022), yet direct evidence of its minimum extent during the HTM remains scarce, largely relying on indirect proxies, and the precise magnitude of ice loss during this period remains an open question (Leger et al., 2024).

Substantial progress in reconstructing the GrIS evolution over the past 22 kyr has been achieved through reliable constraints on ice-sheet extent changes and thickness variations. These include the reconstruction of the time evolution of the ice-sheet extent indicating the timing of margin retreat (the PaleoGrIS v1.0 extent-isochrone reconstruction of Leger et al., 2024), the change in elevation at several ice-core locations (Vinther et al., 2009; Lecavalier et al., 2013), and the relative sea level (RSL) in different regions along the Greenland coast (Gowan, 2023).

Based on these paleoglaciological records, several modeling studies have investigated the GrIS deglaciation using different approaches. Early modeling efforts used RSL reconstructions from many sites along the Greenland margin to constrain ice-sheet extent (Simpson et al., 2009; Lecavalier et al., 2014). These studies successfully reproduced the ice-sheet area evolution over the past 20 kyr. Nevertheless, their volume estimates remained highly uncertain due to coarse spatial resolution, simplified ice dynamics (the shallow-ice approximation), unresolved grounding-line processes, and lack of ice-ocean interactions. Moreover, the former studies showed the difficulties of ice-sheet models to capture ice-sheet elevation changes at Greenland ice cores locations as reconstructed by Vinther et al. (2009).

Tabone et al. (2024) carried out an ensemble simulation of 3,000 members to investigate the role of the Northeast Greenland Ice Stream (NEGIS) in driving Holocene ice-thickness changes recorded at the NGRIP ice core site, demonstrating that NEGIS

https://doi.org/10.5194/egusphere-2026-3331
Preprint. Discussion started: 25 June 2026

dynamics were indeed a primary control on its evolution. However, they did not investigate to what extent their simulations were consistent with other paleo ice-sheet reconstructions.

In a recent study, Lauritzen et al. (2024) demonstrated that, starting from a glacial state in which the GrIS was connected to the Laurentide Ice Sheet (LIS) through an extensive ice shelf covering Baffin Bay, buttressing effects significantly influenced ice-sheet dynamics by allowing the ice to become thicker at the LGM. Subsequently, as this ice shelf was lost during deglaciation, the resulting reduction in surface elevation was substantially amplified. This approach successfully reproduced the elevation changes recorded at ice-core sites documented by Vinther et al. (2009). However, despite achieving good agreement with observed surface elevation changes, this study simulated a retreat 3 kyr later than observed and too large an ice-sheet extent during the Holocene as compared to the PaleoGrIS v1.0 reconstruction (Leger et al., 2024), leaving room for improvement in capturing the ice-sheet retreat.

Leger et al. (2025) represents the first systematic comparison of last-deglaciation simulations against multiple paleo ice-sheet proxies. This comprehensive assessment combines the known maximum LGM extent within existing uncertainty bounds, the timing and spatial heterogeneity of margin retreat through the PaleoGrIS v1.0 extent isochrones (Leger et al., 2024), and present-day ice-sheet observations. However, none of the simulations within their ensemble successfully reproduced all empirical constraints, as model configurations that achieved LGM-consistent ice extent did not accurately represent present-day conditions, and vice versa.

To date, a complete reconstruction of the GrIS through the last deglaciation that simultaneously satisfies constraints on LGM margin extent, the timing and pattern of margin retreat, ice-surface elevation changes at the ice-core sites, and present-day configuration remains elusive. Here we present a detailed analysis of the 3,000-member ensemble of Tabone et al. (2024) with the aim of filling this gap. In the present study, we show that this ensemble additionally contains a simulation that, despite remaining model limitations, achieves a very good agreement with the different observational constraints. We further analyse the evolution of the GrIS through the last deglaciation, quantify its contribution to global mean sea level (GMSL) during the local LGM and the HTM, and identify the key model parameters controlling its evolution, providing insights to improve future representations of this critical period.

2 Methods

2.1 Ice sheet model and simulations ensemble

In this work we use the GrIS deglaciation ensemble simulations described in Tabone et al. (2024), performed with the three-dimensional thermomechanically coupled ice-sheet model Yelmo (Robinson et al., 2020) version 1.801 at 8 km resolution and 6 vertical layers. This version adopts the depth-integrated-viscosity approximation (DIVA) velocity scheme, and a higher-order stress approximation (Lipscomb et al., 2019; Robinson et al., 2022).

For basal friction, the model employs the regularized Coulomb friction law (Joughin et al., 2019):

$$\boldsymbol{\tau}_\mathrm{b} = -\beta\,\mathbf{u}_\mathrm{b} = -C_\mathrm{b}\left(\frac{|\mathbf{u}_\mathrm{b}|}{|\mathbf{u}_\mathrm{b}|+u_0}\right)^q \frac{\mathbf{u}_\mathrm{b}}{|\mathbf{u}_\mathrm{b}|}, \tag{1}$$

https://doi.org/10.5194/egusphere-2026-3331
Preprint. Discussion started: 25 June 2026

where $\mathbf{u}_\mathrm{b}$ is the basal velocity, q is a tunable friction law exponent, $u_0 = 100\,\mathrm{m\,yr^{-1}}$ is the regularization term, and C_b is the yield stress of basal till, defined as:

$$C_\mathrm{b} = \lambda c_\mathrm{f} N_\mathrm{eff}, \tag{2}$$

where N_eff is the effective pressure, c_f is a dimensionless friction coefficient characterizing the local bed properties, and λ is a coefficient that varies exponentially with bedrock elevation (z_b):

$$\lambda = \begin{cases} 1 & \text{if } z_\mathrm{b} > z_1 \\ \max\left[\exp\left(\frac{z_\mathrm{b}-z_1}{z_1-z_0}\right), \lambda_\mathrm{min}\right] & \text{if } z_\mathrm{b} < z_1 \end{cases}, \tag{3}$$

using $z_1 = 400$ m and treating z_0 as an tunable parameter. This formulation reduces the friction and allows for enhanced ice flow in topographically depressed marine regions due to softer till properties (Blasco et al., 2024).

The friction coefficient c_f remains spatially uniform and equal to 1 across the whole domain, except in the northeastern basin, where it has a spatially heterogeneous and time-dependent treatment in order to represent the NEGIS. There, c_f was varied throughout the Holocene within the three NEGIS branches through a scaling factor f ranging between 0 and 1 to reproduce an active northern paleo ice stream during the early to mid-Holocene, a persistent central ice stream, and the development of the present-day southern main branch. This spatial-temporal variability is controlled by two tunable parameters, f_mid and f_min (Fig. S1 in the supplementary material of Tabone et al. (2024)). These parameters simulate the temporal migration of ice-stream activity from the northern paleo-configuration to the modern southern NEGIS geometry and are perturbed across the ensemble to explore uncertainty in basal sliding conditions.

To account for hydrological influences on basal conditions, effective pressure is calculated following Bueler and van Pelt (2015):

$$N_\mathrm{eff} = N_0 \left(\frac{\delta P_0}{N_0}\right)^s 10^{\left(\frac{e_0}{C_c}\right)(1-s)}, \tag{4}$$

where $P_0 = \rho_i g H$ is the ice overburden pressure, $N_0 = 1000\,\mathrm{Pa}$ is a reference effective pressure, e_0 and C_c are empirical constants related to till properties (see Table1), $s = W_\mathrm{til}/W_\mathrm{til}^\mathrm{max}$ is the till saturation, and δ represents a fraction of the overburden pressure and is a tunable parameter in the ensemble.

Calving is parameterized using the von Mises stress criterion following Lipscomb et al. (2019), where the lateral calving rate c is calculated as

$$c = \kappa_T \cdot \tau_\mathrm{ec}, \tag{5}$$

where κ_T is the calving scaling parameter, treated as a tunable parameter in the ensemble, and τ_ec is the effective stress at the ice front.

A flow enhancement factor is incorporated into Glen's flow law to account for ice anisotropy. Regime-specific values are assigned: $E_\mathrm{shelf} = 0.7$ for floating ice, $E_\mathrm{stream} = 1$ for streaming zones, and E_shear the enhancement factor for shearing-driven areas, is treated as a tunable parameter.

https://doi.org/10.5194/egusphere-2026-3331
Preprint. Discussion started: 25 June 2026

Table 1. Summary of the main physical parameters of the model configuration discussed in the text.

Parameter	Description	Value
u_0	Regularization term in the regularized Coulomb friction law	100 m yr^{-1}
z_1	Minimum bedrock elevation to reduce basal friction in topographic depressions	400 m
N_0	Reference effective pressure	1000 Pa
e_0	Reference void ratio at N_0	0.69
C_c	Till compressibility	0.12
E_{shelf}	Enhancement factor for ice-shelf areas	0.7
E_{stream}	Enhancement factor for streaming areas	1
B_{ref}	Reference melting rate for the present-day	1 m yr^{-1}

For glacial isostatic adjustment, the study employs an elastic lithosphere–relaxed asthenosphere (ELRA; Le Meur and Huybrechts, 1996) model. In this framework, the solid Earth is divided into two layers: an elastic lithosphere with spatially homogeneous thickness H_e that responds instantaneously to load-induced compression, and an asthenosphere conceptualized as a viscous half-space that is parameterized by a spatially homogeneous relaxation time τ. Both H_e and τ are tunable parameters in the ensemble.

Surface melting is calculated using an insolation-temperature melt (ITM) scheme (Robinson and Goelzer, 2014):

$$M_{\text{s}} = \frac{\Delta t}{\rho_{\text{w}} L_{\text{m}}} \left[\tau_{\text{a}}(1-\alpha_{\text{s}})\, S + c + \lambda T\right] \tag{6}$$

where Δt is the day length, ρ_w is the water density, L_m is the latent heat of fusion for ice, τ_a is the surface-elevation-dependent atmospheric transmissivity, α_s is the surface albedo, S is the insolation, λ is the long-wave radiation coefficient, T is the air temperature, and c is a latitude-dependent correction term defined as

$$c = c_1 + b(\phi - \phi_0), \tag{7}$$

where c_1 and b are tunable parameters in the ensemble to adjust the SMB, with b scaling the correction relative to a reference latitude $\phi_0 = 65^\circ$ N and ϕ representing the local latitude.

Basal mass balance (BMB) follows an anomaly method, in which the melting in the grounding line is:

$$B_{\text{m}}(t) = B_{\text{ref}} + \kappa\, \Delta T_{\text{ocn}}(t), \tag{8}$$

where $B_{\text{ref}} = 1\text{m}\,\text{yr}^{-1}$ is a reference melting rate for the present-day, ΔT_{ocn} is the paleoclimatic subsurface ocean temperature anomaly around Greenland (see section 2.1.1), and κ is the ice-water heat flux coefficient and is a permutable parameter in the ensemble. BMB is limited to positive values (refreezing is not allowed) and, in agreement with observations of GrIS glaciers (Wilson et al., 2017), sub-shelf melt is 10% of the grounding-line melt.

https://doi.org/10.5194/egusphere-2026-3331
Preprint. Discussion started: 25 June 2026

Table 2. The 13 model parameters varied in the ensemble simulations.

Parameter	Description	Units	Range
Ice dynamics			
f_{mid}	Mid NEGIS basal friction coefficient	–	[0.2, 0.8]
f_{low}	Low NEGIS basal friction coefficient	–	[0.1, 0.4]
q	Friction law exponent	–	[0.5, 1]
z_0	Bedrock e-folding depth for basal friction reduction	m	[-1000, 0]
δ	Fraction of overburden pressure	–	[0.02, 0.06]
E_{shear}	Enhancement factor for the shearing-driven areas	–	[1.0, 1.5]
κ_{T}	Calving scaling parameter	$\mathrm{m\,yr^{-1}\,Pa^{-1}}$	$[5.0{\cdot}10^{-4}, 1.5{\cdot}10^{-3}]$
Atmosphere			
b	Latitude correction for surface melt	$\mathrm{W\,m^{-2}}$	[-3.5, -2.0]
c_1	Additional correction for surface melt	$\mathrm{W\,m^{-2}}$	[-35, -24]
f_{p}	Precipitation scaling factor	-	[0.1, 1.5]
Ocean			
κ	Ocean sensitivity	$\mathrm{m\,yr^{-1}\,K^{-1}}$	[0, 10]
Solid Earth			
H_{e}	Elastic lithosphere thickness	km	[50, 200]
τ	Asthenosphere relaxation time	yr	[500, 3000]

2.1.1 Climate forcing

The model is initialized using a steady-state 50-kyr-long spin-up under LGM conditions. The ice sheet is then forced toward the present using the transient climatologies described below.

Atmospheric temperatures follow an anomaly method and are defined as:

$$T_{\mathrm{atm}}(t) = T_{\mathrm{ref}} + \Delta T_{\mathrm{atm}(t)}, \tag{9}$$

where T_{ref} is the reference temperature, corresponding to the 1981–2010 mean from Box (2013), and ΔT_{atm}(t) are the 2D monthly temperature anomalies from Buizert et al. (2018), obtained by correcting the atmospheric temperature anomalies simulated in the TraCE-21ka fully coupled atmosphere–ocean experiment to account for the reconstructed Atlantic Meridional Overturning Circulation (AMOC) strength variations through the last deglaciation. To account for the evolving ice-sheet topography, we adjust $T_{\mathrm{atm}}(t)$ using a seasonally varying lapse rate that scales temperatures to the current surface elevation of the model.

https://doi.org/10.5194/egusphere-2026-3331
Preprint. Discussion started: 25 June 2026

Precipitation changes are obtained from the high-precipitation scenario in the ice-core-based spatial reconstruction of Badgeley et al. (2020) (high precipitation scenario), applied through the scaling relationship:

$$P(t) = P_{\mathrm{rec}} \cdot \frac{P_{\mathrm{ref}}}{P(t = \mathrm{ref})_{\mathrm{rec}}} \cdot e^{f_p \delta_z \gamma_{\mathrm{atm}}}, \tag{10}$$

where P_{ref} is the reference precipitation field corresponding, as T_{ref}, to the 1981–2010 climatological mean (Box, 2013); $P(t)_{\mathrm{rec}}$ is the time-dependent spatial evolution of precipitation from Badgeley et al. (2020); $P(t = \mathrm{ref})_{\mathrm{rec}}$ is the Badgeley et al. (2020) reconstruction in the reference period (1981–2010); δ_z is the difference in surface elevation between the climatology and the simulation; and γ_{atm} is the atmospheric lapse rate. The parameter f_p is a precipitation scaling factor for past precipitation anomalies. It is a spatially variable parameter; however, here it is considered a tunable parameter only for the northeastern basin and constitutes one of the perturbed parameters of the ensemble.

Subsurface ocean temperatures ΔT_{ocn} are taken from TraCE-21ka (Liu et al., 2009, 2012; He et al., 2013) and averaged at 300–350 m depth, with a uniform correction applied in the northeastern basin to represent the continuous advection of warm Atlantic Water onto the shelf during the early to mid-Holocene, as described in Tabone et al. (2024). Additionally, global sea level is prescribed as a uniform forcing following the reconstruction of Waelbroeck et al. (2002).

The ensemble consists of 3,000 transient simulations spanning the last 22 kyr, in which 13 key parameters (Table 2) are perturbed using Latin hypercube sampling (Stein, 1987). For further details on model physics and experimental setup, see Tabone et al. (2024).

2.2 Past and present observables

Substantial progress has been made in reconstructing the GrIS evolution from the LGM to the present day, providing extensive spatial and temporal observational coverage of ice-sheet changes over the last 22 kyr (Fig. 1). When modeling the GrIS throughout the last deglaciation, we aim to simulate these records as closely as possible while ensuring that simulations converge to a present-day state that is consistent with observations. For this reason, we identify simulations that best approximate the observational constraints summarized in Fig. 1 and described below.

1. **Present-day state**. To evaluate the present-day ice-sheet configuration, we compare simulated fields against the ice thickness, ice cover and bedrock elevation measurements from the BedMachine version 5 dataset (Morlighem et al., 2017), and against the surface velocity of Joughin et al. (2018).

2. **Elevation changes**. Vinther et al. (2009) reconstructed Holocene surface elevation changes at four ice core sites — Camp Century, NGRIP, GRIP, and DYE-3 — by analysing $\delta^{18}O$ isotope records (Fig. 1c). Their analysis assumed that elevations in the marginal ice caps remained constant throughout the Holocene, allowing them to extract the temperature signal from these. Assuming this signal was uniform throughout the GrIS, they were able to reconstruct the elevation change at the remaining ice-core locations by removing the temperature signal. Their findings demonstrated that the initial response to Holocene conditions was an elevation increase at all locations, attributed to enhanced precipitation and bedrock uplift. Subsequently, significant thinning occurred at the coastal locations (Camp Century and DYE-3), with this signal propagating inland and affecting the GRIP location approximately 4 kyr after the onset of the Holocene.

https://doi.org/10.5194/egusphere-2026-3331
Preprint. Discussion started: 25 June 2026

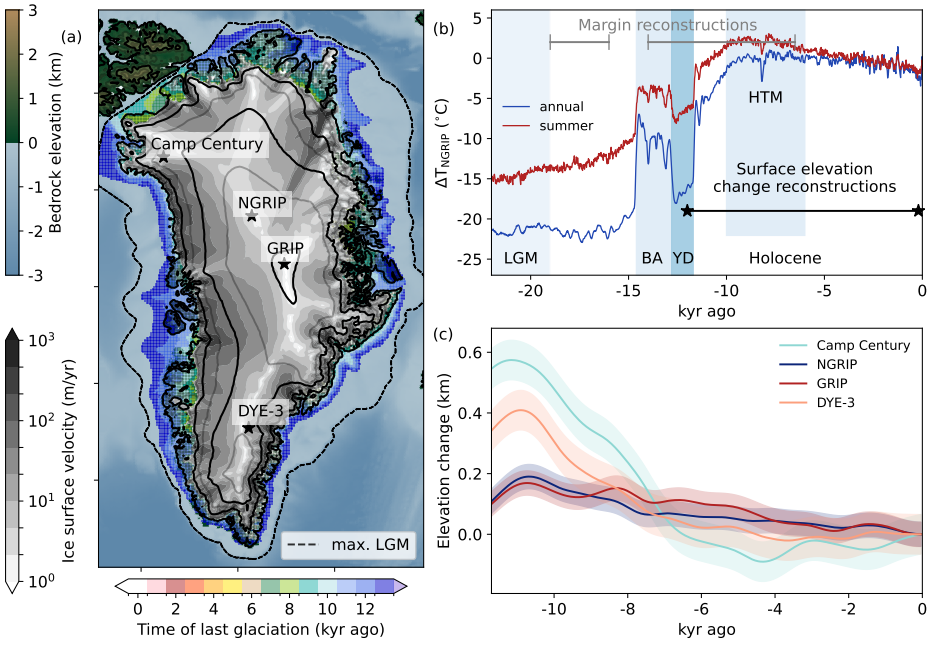

Figure 1. (a) Summary of the observational constraints used in this study: present-day GrIS surface velocities (Joughin et al., 2018) overlaid on bedrock elevation (Morlighem et al., 2017), and ice surface elevation in black and gray contours at 1000 and 500 m intervals, respectively (Morlighem et al., 2017). Black stars indicate the four ice-core locations at which surface-elevation changes were reconstructed by Vinther et al. (2009). The colored margin isochrones from the PaleoGrIS v1.0 dataset (Leger et al., 2024) show the time of last glaciation at each location — that is, the most recent time at which each point was covered by grounded ice. The black line marks the continental-shelf break, with the maximum LGM grounded extent estimated to lie between this line and the first isochrone, corresponding to 13 kyr ago (Leger et al., 2025). (b) Annual and summer temperature anomaly at NGRIP relative to present day, following Buizert et al. (2018). Key climatic periods are indicated: the Last Glacial Maximum (LGM: ∼26–19 kyr ago), the Bølling–Allerød warming (BA: 14.6–12.8 kyr ago), the Younger Dryas cold reversal (YD: 12.8–11.7 kyr ago), the Holocene (11.7 kyr ago to the present-day) and the Holocene Thermal Maximum (HTM: 10–6 kyr ago). Grey and black horizontal lines indicate the time coverage of the margin and the surface-elevation change reconstructions, respectively (also marked in the lower panel). (c) Elevation change reconstruction at the ice-core locations with its uncertainty (Vinther et al., 2009).

3. **The timing of margin retreat**. We use the PaleoGrIS v1.0 dataset of Leger et al. (2024), an empirical reconstruction of GrIS-margin locations derived from geomorphological and geochronological evidence. The dataset documents the
185 spatially heterogeneous retreat of ice margins across Greenland during the Late Glacial and early-to-mid Holocene periods, spanning approximately 13.0 to 6.5 kyr ago (Fig. 1b), and provides 500-year resolution isochrone buffers. Here, as in Leger et al. (2024), an isochrone refers to a contour delineating the ice sheet margin at a given point in time — more precisely, it marks the most recent time at which each location was still covered by grounded ice.

https://doi.org/10.5194/egusphere-2026-3331
Preprint. Discussion started: 25 June 2026

Table 3. Summary of the observational metrics used for the scoring.

Score	Observable	Original data for comparison
S_H	H (present-day ice thickness)	BedMachine v3 (Morlighem et al., 2017)
$S_{\text{ice cover}}$	f_{ice} (present-day ice mask/cover)	BedMachine v3 (Morlighem et al., 2017)
$S_{z\,bed}$	z_{bed} (present-day bedrock elevation)	BedMachine v3 (Morlighem et al., 2017)
S_u	u (present-day surface velocities)	GIMP (Joughin et al., 2018)
S_{iso}	iso (extent-isochrones, i.e., margin retreat)	PaleoGrIS v1.0 (Leger et al., 2024)
S_{GRIP}	GRIP (elevation change at GRIP)	Vinther et al. (2009)
S_{NGRIP}	NGRIP (elevation change at NGRIP)	Vinther et al. (2009)
S_{DYE3}	DYE3 (elevation change at DYE-3)	Vinther et al. (2009)
S_{LGM}	LGM (LGM maximum ice extension)	Mask between continental-shelf break and first isochrone
S	Global weighted score	

4. **The LGM**. As discussed by Sbarra et al. (2022), the maximum extent of the GrIS during the LGM is poorly constrained, with reconstructions varying between an inner continental-shelf minimum, a mid-shelf position, and a maximum extent at the shelf break. Hence, to constrain the LGM maximum extent, we adopt the approach of Leger et al. (2025), assuming that the maximum grounded-ice extent lies between the continental-shelf break and the first retreat extent isochrone, 13 kyr ago (region between black and dark-blue lines in Fig.1a).

2.3 Validation process

Following previous studies (Whitehouse et al., 2012; Pollard et al., 2016), we compare each simulation j with each observable i (Table 3), obtaining a misfit M_i^j for each simulation j with respect to each observable i. Unless otherwise stated, each misfit is defined as the mean squared residual normalised by the observational uncertainty, as follows:

$$M_i^j = \frac{1}{N}\sum_{k=1}^{N}\left(\frac{\hat{i}_k^j - i_k}{\sigma_{ik}}\right)^2, \tag{11}$$

where N is the total number of grid cells in the domain; $\hat{i}_k^j$ is the modeled value of variable i at grid cell k in simulation j; and i_k and σ_{ik} denote the observed value and uncertainty of variable i at grid cell k, respectively. Since the observational uncertainty can be very small in some grid cells for certain metrics, we follow Pollard et al. (2016) and define an acceptable model error for these data types. This allows us to represent the typical difference between model output and observations in reasonably good simulations, while also preventing misfits to be very bad for all runs, including misfits that tend to infinity at locations where instrumental precision is very high and observational errors are very small. Thus, σ_{ik} is defined as:

$$\sigma_{ik} = \max(\sigma_{ik}^{\text{obs}}, \sigma_i^{\text{min}}), \tag{12}$$

https://doi.org/10.5194/egusphere-2026-3331
Preprint. Discussion started: 25 June 2026

where $\sigma_{ik}^{\mathrm{obs}}$ is the observational uncertainty for data type i at the grid cell k, and σ_i^{min} is the acceptable model error for data type i.

For the present-day ice thickness ($i = \mathrm{H}$), present-day bedrock elevation ($i = z_{\mathrm{bed}}$) and present-day ice-cover ($i = f_{\mathrm{ice}}$), observations and observational uncertainties are taken from Morlighem et al. (2017) and we consider $\sigma_i^{\mathrm{min}} = 10\,\mathrm{m}$ as in Pollard et al. (2016) for M_{H} and $M_{z\,\mathrm{bed}}$. f_{ice} is a binary variable with $f_{\mathrm{ice}} = 1$ where ice is present and $f_{\mathrm{ice}} = 0$ otherwise. Therefore, for this variable, no uncertainty normalization is applied, i.e., $\sigma_{ik} = 1$. For present-day ice surface velocity ($i = u$), observations and uncertainties are taken from Joughin et al. (2018), and we set $\sigma_u^{\mathrm{min}} = 1\,\mathrm{m\,yr^{-1}}$ as a demanding threshold for what would constitute a good agreement between model and observations.

For the paleo state, the deglaciation-isochrone misfit (M_{iso}^j), based on the PaleoGrIS v1.0 dataset of Leger et al. (2024), follows the definition from Eq.11, with the modeled isochrone at each grid cell being defined as the last time step at which that cell was glaciated. The surface-elevation evolution misfit (M_{NGRIP}^j, M_{GRIP}^j, and M_{DYE3}^j) is defined analogously to Eq.11, but with the sum iterating over times steps $t = 1 \ldots T$, where T is the total number of time steps at which observations are available:

$$M_i^j = \frac{1}{T} \sum_{t=1}^{T} \left(\frac{\hat{i}_t^j - i_t}{\sigma_{it}} \right)^2 . \tag{13}$$

The misfit between modeled and observed elevation change is computed for each of the three ice-core locations, NGRIP, GRIP and DYE-3, with observations and uncertainties taken from Vinther et al. (2009). Note that the Camp Century surface elevation record is excluded from the misfit and score computation, since no simulation within the ensemble is able to reproduce the observed changes at this location, as discussed in Section 3.1.

Lastly, M_{LGM}^j is the grounding-line misfit at the LGM, based on the maximum local LGM ice extent of Leger et al. (2025), spanning the interval from 19 to 16 kyr ago. Unlike the other misfits, M_{LGM}^j measures the fraction of grounding-line grid cells lying outside the LGM mask, averaged over this interval. By construction, $M_{\mathrm{LGM}}^j = 0$ when the grounding line lies entirely within the mask at all sampled time steps, and $M_{\mathrm{LGM}}^j = 1$ when it lies entirely outside.

Once all individual misfits M_i^j are computed for every simulation j, they are normalized by the median misfit across the ensemble for each observable,

$$M_i^{j\prime} = \frac{M_i^j}{M_i^{50}}, \tag{14}$$

where M_{50}^i is the median of M_i over all simulations j. This normalization ensures that each observable i contributes equally to the aggregate score, regardless of the absolute magnitude of its misfit. Next, to compute the aggregate score over observables, each normalized misfit (for every simulation j) is first converted into an individual score via an exponential decay:

$$S_i^j = e^{-M_i^{j\prime}}, \tag{15}$$

https://doi.org/10.5194/egusphere-2026-3331
Preprint. Discussion started: 25 June 2026

so that $S_j^j \in (0,1]$, with $S_i^j = 1$ for a perfect fit and $S_i^j \to 0$ as the misfit grows. Finally, the aggregate or global score for each simulation j is defined as the product of all individual scores:

$$S^j = \prod_{i=1}^{9} S_i^j = e^{-\sum_{i=1}^{9} M_i^{j\prime}}, \quad j = 1, ..., 3000 \tag{16}$$

which is equivalent to weighting simulations by the exponential of the total normalized misfit. Simulations with S^j closer to 1 provide a better overall agreement with the observational constraints. We refer to the global score of the simulations as S below. All the scores are summarized in Table 3.

3 Results

3.1 Ensemble evaluation against observational constraints

Fig. 2 illustrates the ensemble evolution over the last 22 kyr. Regarding the grounded area and volume (Fig. 2b–c), all simulations show a very similar behavior: a modest increase in both quantities between 22 and 15 kyr ago, followed by a pronounced decrease associated with the Bølling–Allerød warming. Although ice loss decelerates during the Younger Dryas cooling interval, the ice sheet continues to retreat until approximately 7–5 kyr ago. At this point, the spread of the simulations is larger, with some simulations showing ice-sheet retreat well beyond the present-day margin, while others maintain grounded areas and volumes exceeding the present-day state. Subsequently, simulations show a slight regrowth driven by the cooling following the HTM. The largest ensemble spread in both grounded area and volume occurs during the LGM and throughout the Holocene, while the rapid retreat between approximately 15 and 10 kyr ago is characterized by a notably coherent response across all members, especially the ones with higher scores. The best simulation (black line) shows excellent agreement with the observed grounded area from Leger et al. (2024), remaining within the observational uncertainty bounds throughout the period covered by the data.

Regarding surface air temperature over the ocean surrounding Greenland (Fig. 2a), differences among ensemble members (yellow-to-green lines) are generally small, as expected given that temperature constitutes the primary forcing of the ice-sheet model. However, these differences are larger before 15 kyr ago, reflecting the greater spread in ice-sheet extent during the LGM: smaller ice sheets result in a wider ocean domain, which varies across ensemble members — and therefore so does the domain-averaged temperature — whereas once the ice sheet retreats to its interior the ocean domain remains effectively constant across simulations.

Following the hydrological basin delineation of Mouginot et al. (2019), the GrIS domain is divided into seven distinct regions, with basin boundaries extended to include the maximum LGM ice-sheet extent, following previous studies (Leger et al., 2025; Lauritzen et al., 2024). The simulated evolution of the grounded area within each region, alongside the reconstructed area derived from the PaleoGrIS v1.0 margin isochrones, is shown in Fig. 3. Overall, the simulations show good agreement with the reconstructed retreat across most regions. Two notable exceptions are identified: in the southwestern (SW) basin, where the simulated retreat begins earlier and is more extensive than reconstructed during the early Holocene; and in the eastern (E)

https://doi.org/10.5194/egusphere-2026-3331
Preprint. Discussion started: 25 June 2026

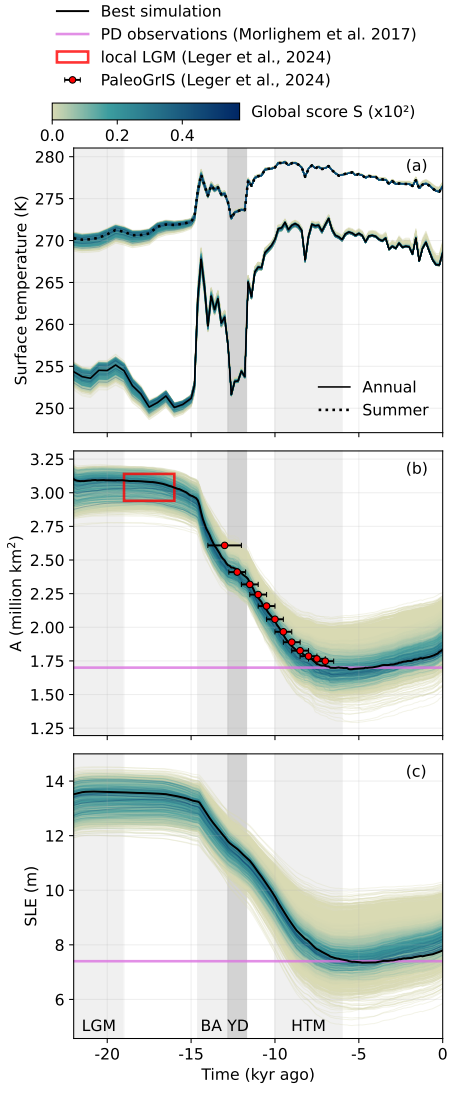

Figure 2. : (a) Mean annual (solid lines) and summer (dotted lines) surface air temperature over the ocean surrounding Greenland (Buizert et al., 2018, reconstruction with a topographic correction as explained in Sec. 2.1.1). (b) Time series of grounded ice-sheet area for all ensemble members (colored lines) and the best-scoring simulation (black line), deglacial history from PaleoGrIS v1.0 (red dots, Leger et al., 2024), and a red open rectangle indicating the timing and extent of the local LGM (Leger et al., 2024, from literature review). (c) Ice volume in sea-level equivalent (m SLE) for all ensemble members (colored lines) and the best-scoring simulation (black line). Line colors indicate the global score S of each simulation. The pink line indicates present-day values (Morlighem et al., 2017).

basin, where the simulated margin retreat occurs approximately 2.5 kyr earlier than recorded in the PaleoGrIS v1.0 dataset.

https://doi.org/10.5194/egusphere-2026-3331
Preprint. Discussion started: 25 June 2026

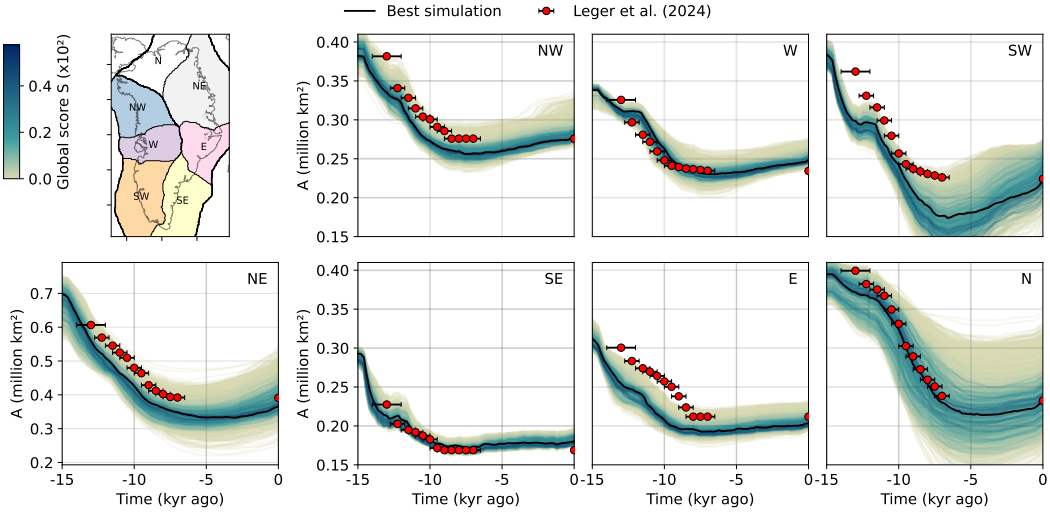

Figure 3. Grounded area of the ensemble simulation against the PaleoGrIS v1.0 reconstruction (Leger et al., 2024) for the last 15 kyr. The area is divided into the seven regions indicated in the first panel, following the present-day glacier catchment basins (Mouginot et al., 2019). The color of the lines indicates the score S of each simulation, the best simulation is marked in black and the red dots indicate the area following PaleoGrIS.

While all ensemble members exhibit a broadly similar retreat pattern, these regions are prone to a systematically earlier retreat relative to the reconstructions.

Fig. 4 shows the evolution of ice-surface elevation at the four ice-core locations over the Holocene (NGRIP, GRIP, Camp Century and DYE-3), compared against observational records used to derive the scores S_{NGRIP}, S_{GRIP}, and $S_{\mathrm{DYE-3}}$ (Vinther et al., 2009). The ensemble shows a large inter-member spread, with elevation differences of up to 1000 m at DYE-3 and on the order of 200–400 m at the remaining locations. The expected behavior, according to the reconstruction, consists of an initial thickening at the onset of the Holocene driven by enhanced accumulation in response to rising temperatures and/or bedrock uplift (Vinther et al., 2009), followed by progressive thinning toward present-day ice thickness.

At NGRIP and GRIP — two locations in the central GrIS separated by approximately 300 km — the best-performing simulation achieves a good fit to observations, with scores of 0.88 and 0.77, respectively and simulated elevations remaining within observational uncertainty throughout most of the period. In both cases, the simulations with the highest global score S are also those that best match the observational records, particularly at NGRIP. This is consistent with the fact that the ensemble was originally designed to reproduce the thinning signal at this location.

At DYE-3, located more than 800 km south of GRIP in a more marginal sector of the ice sheet characterized by lower surface elevations, the fit to observations remains acceptable, although less accurate than at the central dome sites. The observed record indicates that elevations should have been 200 m higher at the onset of the Holocene, with a thinning of approximately 400 m over the first 4 kyr of the Holocene, followed by relative stability thereafter. In contrast, the ensemble simulates substantially

https://doi.org/10.5194/egusphere-2026-3331
Preprint. Discussion started: 25 June 2026

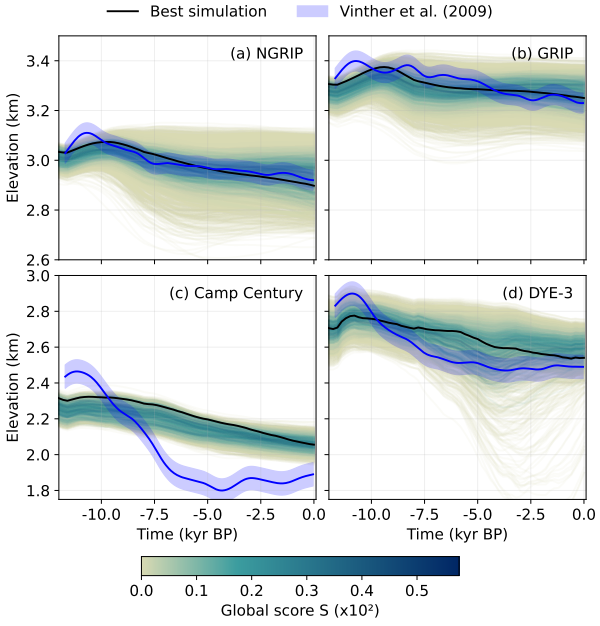

Figure 4. Surface elevation at the ice-core locations of the whole ensemble simulations with the color of the lines indicating the score S of each simulation, the best simulation in black, and the Vinther et al. (2009) reconstruction with its uncertainty in blue.

smaller thickness changes — on the order of 200 m — distributed more gradually across the Holocene. Consequently, the best-performing simulation achieves a score of approximately $S_{\mathrm{DYE-3}} = 0.56$ at this location, somewhat lower than those obtained at NGRIP and GRIP.

At Camp Century, the most marginal of the four locations, situated approximately 150 km away from the present-day coastline, ice-thickness changes during the last deglaciation were particularly large, as the site transitioned from an interior to a near-marginal position with an elevation change of nearly 700 m over 6 kyr. In the simulations, Camp Century is indeed the location with the largest modeled elevation changes (approximately 300 m); however, none of the ensemble members adequately captures the observed signal. In all simulations, the ice is too thin at the beginning of the Holocene and too thick at the end. Given the consistently poor performance of the ensemble in reproducing elevation changes at this location, the corresponding score term for Camp Century was excluded from the global score S.

3.2 The GrIS throughout the last deglaciation: best simulation

The evolution of the GrIS best-fit simulation over the last 20 kyr is represented in Fig. 5, which shows the ice-sheet topography, ice-surface velocities, and ice-surface elevation, together with the PaleoGrIS v1.0 ice-margin reconstruction and the continental shelf-break (Leger et al., 2025). The corresponding parameter values, selected by maximizing the global S across the ensemble, are summarized in Table 4.

https://doi.org/10.5194/egusphere-2026-3331
Preprint. Discussion started: 25 June 2026

Param.	Value	Param.	Value
f_{mid}	0.6117	b	-2.2982 W m^{-2}
f_{low}	0.3144	c_1	-30.4856 W m^{-2}
q	0.9072	f_p	0.2408
z_0	-625.9 m	κ	7.167 m yr^{-1} K^{-1}
δ	0.0241	H_e	158.51 km
E_{shear}	1.0037	τ	619.5 yr
κ_T	0.0009		

Table 4. Parameter values of the best-fit simulation.

During the LGM (Fig. 5b), the best-fit simulation yields an ice-sheet volume anomaly of 5.75 m SLE relative to the present-day value in the same simulation, with the ice margin reaching the continental shelf along most of the coastline. A large ice shelf extends through Baffin Bay, fed by a series of fast-flowing ice streams. In contrast, smaller ice shelves are present along the southwestern margin, where steeper surface slopes reflect the influence of the regional mountain ranges. In addition, the GrIS is connected to northern Canada through a bridge to Ellesmere Island. Comparison of the simulated grounding line with the LGM mask reveals good agreement along most of the coastline, with the grounding line falling within the prescribed uncertainty bounds in all regions except the northwest, where the simulated connection with northern Canada appears too restricted in extent. Between 20 and 15 kyr ago, annual mean temperatures remained stable or below previous values (Fig. 1b), while summer temperatures began a gradual rise of approximately 5°C as recorded in the NGRIP ice core. Although the net effect on total grounded ice volume was negligible, this forcing drove several changes along the ice-sheet margin of the best simulation. Widespread retreat and loss of ice shelves occurred across the entire coastline, most prominently in the northwest, accompanied by a corresponding increase in ice surface velocities in the marginal zones.

The most pronounced changes follow the onset of the Bølling–Allerød interstadial ∼14.5 kyr ago, when the mean surface air temperature over the ocean surrounding Greenland increased by approximately 20 °C (Fig. 2a) and around 10 °C in NGRIP (Buizert et al., 2018). By 13 kyr ago (Fig. 5c–d), the ice sheet undergoes pronounced changes, marked by the complete loss of ice shelves and grounding-line retreat along the entire margin. The ice sheet continues to retreat, progressively losing contact with the ocean in certain regions, such as the eastern margin (Fig. 5e). Thereafter, the bridge to Ellesmere Island thins and retreats, gradually reducing this connection. By 9 kyr ago, the GrIS reaches an extent close to that of the present day, with its margin located slightly further inland in the southeast and in the NEGIS region, and maintaining a small connection with Ellesmere Island (Fig. 5f). At 7.6 kyr ago, the Nares Strait opens fully, completely detaching from the island. Between 9 and 7 kyr ago, HTM conditions drive a further retreat of the ice margin behind its present-day position, reaching the minimum ice extent at approximately 5 kyr ago (Fig. 5g). This period is discussed in greater detail in Sec. 3.2.1. Finally, as temperatures decline, both the grounded area and total ice volume increase, recovering towards the present-day configuration (Fig. 5h), as discussed in Sec. 3.2.2.

https://doi.org/10.5194/egusphere-2026-3331
Preprint. Discussion started: 25 June 2026

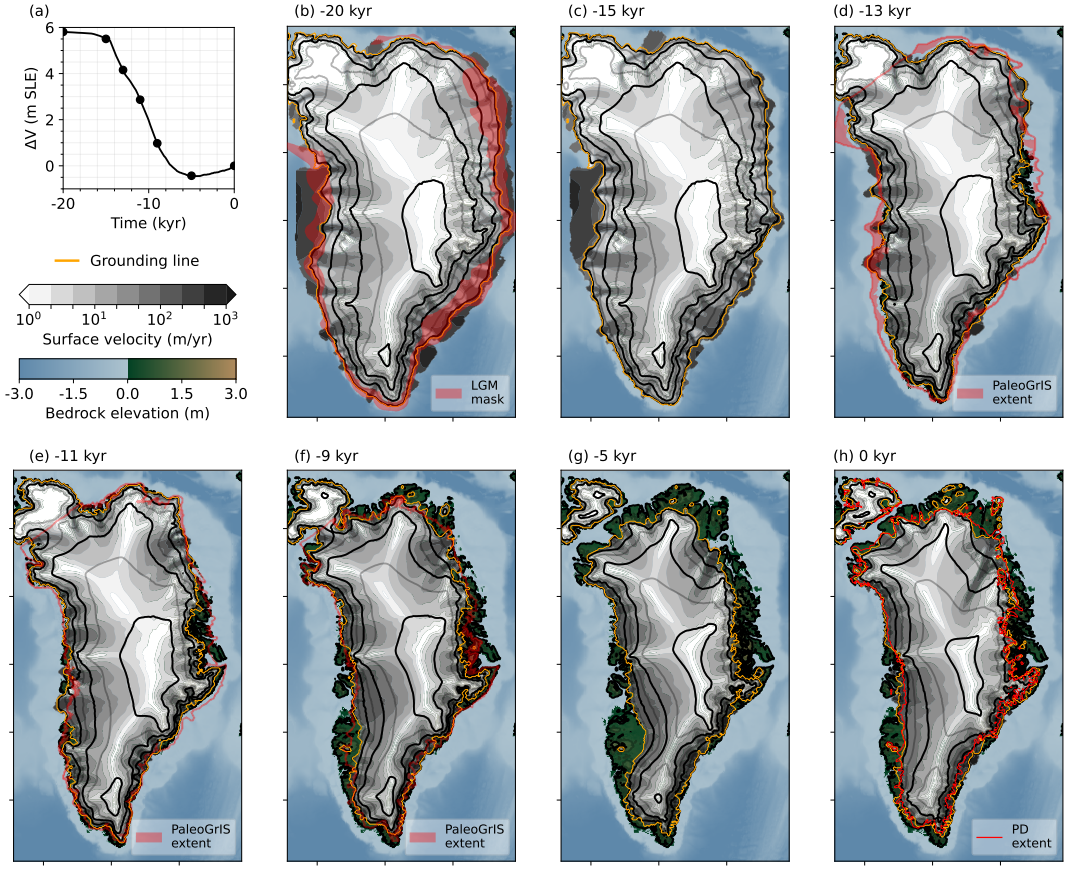

Figure 5. Best simulation evolution. (a) Time evolution of GrIS sea-level equivalent. Dots mark the time slices shown in panels (b)–(h). (b–h) GrIS configuration at different time slices. Grayscale shading shows ice-surface velocity. The red shading in (b) indicates the maximum possible LGM extent identified by Leger et al. (2025). Red solid lines show (d–f) ice-sheet margins from Leger et al. (2024) reconstructions at 13, 11, and 9 kyr ago; (h) present-day observations from Morlighem et al. (2017). Time slices without red lines indicate periods where margin reconstructions are not available. Black contours show ice surface elevation at 1000 m intervals; thin gray contours at 500 m intervals; and the orange contour indicates the simulated grounding line.

Fig. 6 shows a comparison of ice-margin isochrones between the best-fit simulation and the PaleoGrIS v1.0 dataset (Leger et al., 2024). Regarding the temporal coverage of the observational dataset, the oldest isochrone available in PaleoGrIS v1.0 corresponds to 13 kyr ago (Fig. 6a), as margin reconstructions before this period are either spatially incomplete or associated with sufficiently large uncertainties to preclude their inclusion in the dataset. To provide context for this earlier period, the best-fit simulation (Fig. 6b) includes the reconstructed grounded-ice margin before 13 kyr ago (shown in purple), which indicates that the ice margin was located between the 13 kyr ago isochrone and the maximum possible extent (that coincides with the continental-shelf break). This is consistent with geological evidence suggesting that the GrIS reached or approached the shelf

https://doi.org/10.5194/egusphere-2026-3331
Preprint. Discussion started: 25 June 2026

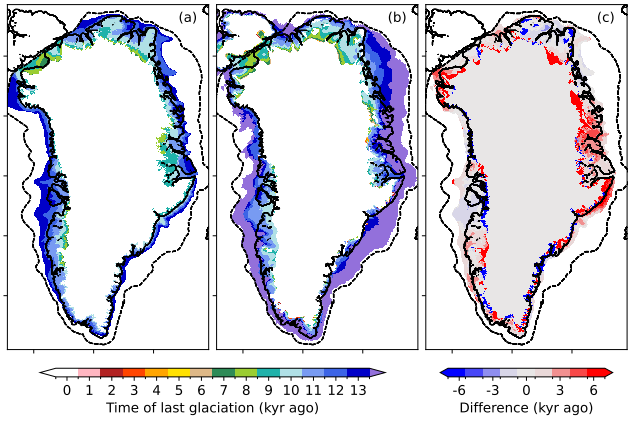

Figure 6. Isochrones in (a) the PaleoGrIS v1.0 reconstruction from Leger et al. (2024) and (b) the best simulation of the ensemble. The colorbar in (a) and (b) shows the last time each grid cell was covered by grounded ice. (c) Difference between our best simulation and isochrones in PaleoGrIS: red (blue) colors indicate an early (late) deglaciation in the best simulation compared with observations. The dashed black line indicates the continental-shelf break.

break during the LGM (Evans et al., 2009; Lecavalier et al., 2014; Arndt et al., 2017; Bradley et al., 2018; Buizert et al., 2018; Tabone et al., 2018; Leger et al., 2024, 2025). Although uncertainties associated with pre-13 kyr ago reconstructions preclude a direct comparison, the simulated margin position remains within the range of plausible extents for this period, lying between the oldest available isochrone and the continental-shelf break, which lends confidence to the model performance during the early deglaciation.

Overall, the simulated margin evolution is in broad agreement with the observational constraints, as can also be seen in Fig. 5, where the simulated ice extent is compared against the PaleoGrIS v1.0 margin positions (red outlines). However, several regional discrepancies exist. The most notable are: (i) an overestimated inland retreat to the north and west of the NEGIS as noted in 3.2.2, (ii) an early-than-observed retreat on the west coast suggesting that the model may be marginally more sensitive to oceanic or atmospheric forcing in these regions, and (iii) a slightly later-than-observed retreat along the central eastern margin and the southwestern coast.

3.2.1 Minimal extension during the HTM

In Fig.7a–b we show the mean climatology during the HTM (10–6 kyr ago, following Buizert et al. (2018)). This is the forcing of the model, i.e., the temperature from Buizert et al. (2018) and precipitation fields from Badgeley et al. (2020), both corrected by the simulated topography. Summer temperatures were higher than present across the entire domain, with a mean anomaly of +2.1 °C over the ocean surrounding Greenland relative to the reference period (1981–2010). This warming was particularly pronounced along the western margin and in the north. Precipitation patterns also differed from the present day, with increased accumulation across the western margin and reduced precipitation over the southeastern margin.

https://doi.org/10.5194/egusphere-2026-3331
Preprint. Discussion started: 25 June 2026

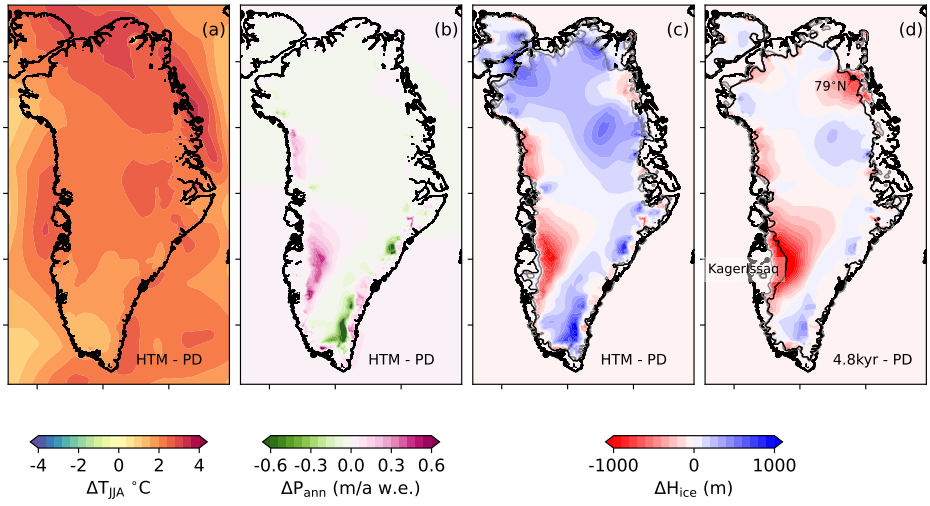

Figure 7. (a)-(c) Differences between the HTM and the simulated present-day state in summer temperature at the sea level, annual precipitation, and ice thickness, respectively. The HTM period is defined following Buizert et al. (2018) as the mean over the interval from 10 to 6 kyr ago. (d) Ice-thickness anomaly at the minimum GrIS extent (i.e., 4.8 kyr ago) relative to the present-day state. Thin black contours indicate the ice-sheet margin of the simulated present-day state; the thick black contour in (c) and (d) indicates the ice margin during the HTM and at the time of minimum extent, respectively; and the grey line indicates the ice margin of the simulated present-day state.

These climatic conditions drove an ice-sheet retreat that, in the best-fit simulation, results in a thinner ice sheet along the western margin relative to present day over the 4 kyr duration of the HTM period (Fig. 7c). Nevertheless, the total ice volume remained greater than at present, as the ice sheet was retreating from a previously expanded state with greater overall ice extent, including a grounded ice connection with Ellesmere Island.

The maximum impact of HTM warming on ice sheet geometry, however, occurs with a lag of approximately 3 kyr relative to the summer temperature peak: the best-fit simulation reaches its minimum extent throughout the last deglaciation at 4.8 kyr ago — roughly 3 kyr after the thermal maximum, 7.8 kyr ago — with a total volume 0.45 m SLE below the present-day state (Fig. 7d). The most significant differences with respect to present day are found along the western margin, in the Kangerlussuaq region, where the ice retreated by up to 100 km in some locations, with thinning propagating inland. A notable retreat of up to 40 km is also simulated along the northeastern margin, in the region drained by the NEGIS, although the 79° North glacier retreats considerably further, reaching a maximum of 140 km.

At this point in time (4.8 kyr ago), surface elevations at ice-core locations (Fig. 4) show good agreement between the best simulation and the reconstructed elevations at NGRIP and GRIP, with a slight excess of ice in the best simulation at DYE-3 (approximately 100 m), and an overestimation of the surface elevation at Camp Century.

https://doi.org/10.5194/egusphere-2026-3331
Preprint. Discussion started: 25 June 2026

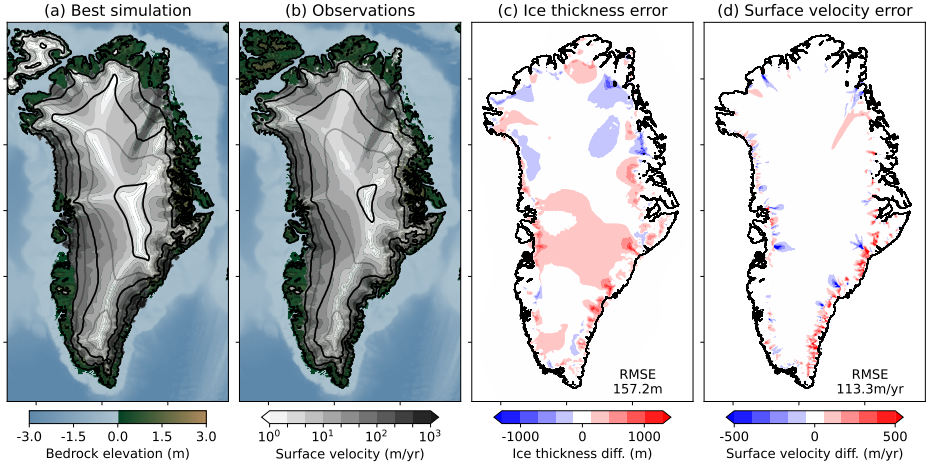

Figure 8. Ice surface velocity and ice surface elevation contours for (a) the best-fitting ensemble simulation and (b) observations (Morlighem et al., 2017; Joughin et al., 2019). Black and gray contours show ice surface elevation at 1000 and 500 m intervals, respectively. (c) and (d) show the ice thickness and ice surface velocities difference between the best simulation and present-day observations.

3.2.2 Present-day performance

Next we compare the final state of the best-fit simulation with present-day observations (Fig. 8). The simulated ice sheet has a total volume of 7.80 m SLE and a grounded area of 1.83×10^6 km^2, which are respectively 5% and 7% above the observed present-day values. The root-mean-square error in ice thickness is 157.2 m, a notably good result given that this is the outcome of a transient simulation spanning the full deglaciation from the LGM.

The overall agreement with present-day observations is good, with discrepancies largely confined to specific regions. Along the southern margins, the ice extent is slightly overestimated, which we attribute to the presence of narrow fjords that are not resolved at the 8-km horizontal resolution of the model. This excess ice propagates inland into the south-central region. This is a well-known limitation of GrIS modelling at this and lower resolutions as has been identified in different studies (Stone et al., 2010; Robinson et al., 2012; Born and Nisancioglu, 2012; Tabone et al., 2018; Höning et al., 2023; Gutiérrez-González et al., 2026a); however, an 8 km resolution remains necessary to make transient ensemble simulations spanning 22 kyr computationally feasible. A second area of discrepancy is found in the region surrounding Danmark Fjord, where the simulated margin lies 15–50 km upstream of the observed position. This retreat can be traced back to the onset of the Holocene (Fig. 5f), suggesting that the margin recession may already be overestimated at that time. In addition, ice thickness in the interior of this region is slightly underestimated, likely as a result of marginally elevated ice-stream velocities.

The simulated velocity field is generally in good agreement with observations across the entire domain, with a satisfactory representation of the NEGIS, consistent with the best-fit simulation of Tabone et al. (2024), and a root-mean-squared-error of 113.3 m·yr^{-1}. The main discrepancies are a slight overestimation of ice velocities within the NEGIS and along the southeastern margin, where the slightly advanced ice extent displaces the fast-flowing regions further seaward relative to observations.

https://doi.org/10.5194/egusphere-2026-3331
Preprint. Discussion started: 25 June 2026

3.3 Insights for a better representation of the deglaciation

Fig. 9 summarizes the individual scores and the global score S computed for each ensemble member. The individual scores are broadly distributed from near-zero up to values on the order of 0.8 for S_{GRIP}, S_{NGRIP}, $S_{\mathrm{z\,bed}}$, and up to 0.5–0.6 for the remaining metrics. An exception is the area-based metrics at distinct time slices (S_{iso}, $S_{\mathrm{ice\,cover}}$, and S_{LGM}), which remain mainly above 0.1–0.2 and below 0.5. However, it is important to emphasize that because the misfits have been normalized by its ensemble median, they are not directly comparable in absolute terms. For a given simulation, a higher value in one score relative to another does not necessarily imply a better absolute performance in that specific metric. Rather, it indicates better performance relative to the rest of the ensemble members.

Aggregating the individual scores into a global score S yields generally low values, as a single poorly performing individual score substantially reduces S, effectively discarding that simulation from the top-performing ensemble members. As a result, only approximately 2% of the simulations (52 in total) achieve $S > 0.002$.

Fig. 10 shows the linear correlations between pairs of individual scores, as well as with S. All present-day metrics (S_{H}, $S_{\mathrm{z\,bed}}$, $S_{\mathrm{ice\,cover}}$, and S_{u}) show positive inter-correlations exceeding 0.2 (except for S_{u} with S_{H}), as well as positive correlations with S, indicating that simulations that adequately reproduce one present-day metric tend to do so for the others as well. Among these, the ice-cover and the isochrones scores play a central role: a good representation of the past and present-day ice extent is strongly associated with an adequate reproduction of present-day ice thickness, bedrock elevation, and surface velocities. This is not the case for the retreat scores (S_{NGRIP}, S_{GRIP}, $S_{\mathrm{DYE-3}}$, and S_{iso}), where the parameter combinations that allow certain glaciological features to be reproduced do not allow the reproduction of others. However, S_{NGRIP} and S_{GRIP} are strongly positively correlated, likely due to their vicinity (only 300 km) and both being in the central part of the ice sheet.

Finally, the LGM score S_{LGM} is largely independent of all other metrics: an accurate reproduction of the LGM margin has little bearing on the subsequent deglaciation or on the present-day state, since, regardless of the LGM extent, the retreat occurs rapidly across all simulations once temperatures rise during the Bølling–Allerød.

To assess the sensitivity of the GrIS deglaciation to the ensemble parameter values, Fig. 11 presents the correlation-coefficient matrix between the evaluated scores and the model parameters. Several features can be extracted from this figure. First, the global score (S), the scores related to the present-day state (S_{H}, S_{ice}, S_{z}, S_{u}), and the isochrone-based score (S_{iso}) are all significantly influenced by the SMB correction parameters: both the latitude-dependent correction term b and the spatially constant correction term c_1 from Eq.6. Increasing these corrections within the explored parameter range leads to improved performance in reproducing the present-day ice-sheet state and the temporal evolution of the ice margin. The precipitation scaling factor f_p, the other parameter directly involved in SMB, shows negligible correlation with any of the evaluated scores. This is not surprising, as f_p is only varied within the northeastern basin and therefore has a limited impact on the broader ice-sheet geometry.

Regarding other climate forcing parameters, the ocean sensitivity κ shows a comparatively large impact on simulation performance. Higher values of κ improve the ice-cover score for both the present day ($S_{\mathrm{ice\,cover}}$) and its temporal evolution throughout the deglaciation (S_{iso}). Furthermore, ocean sensitivity shows a high correlation (0.76) with present-day ice surface

https://doi.org/10.5194/egusphere-2026-3331
Preprint. Discussion started: 25 June 2026

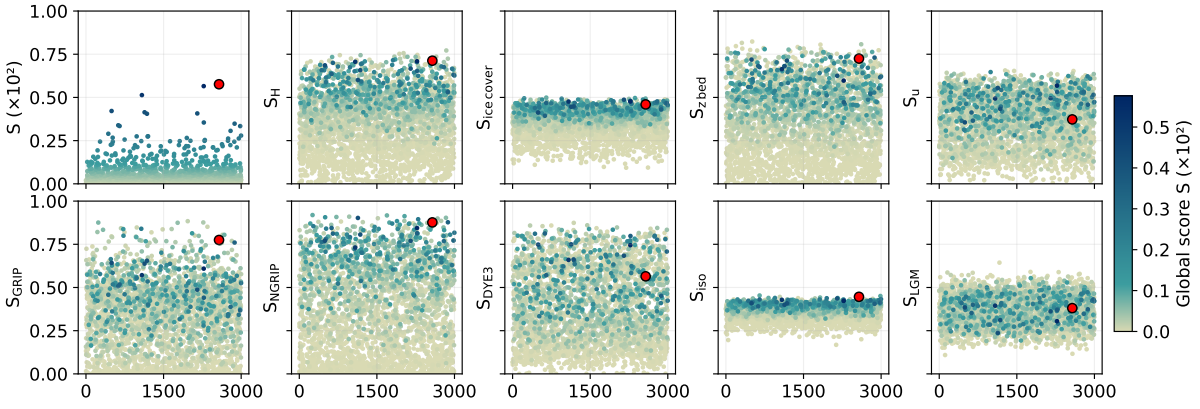

Figure 9. Value of the global score S and the individual scores (ice thickness, ice cover, bedrock elevation, ice surface velocities, surface elevation change at the ice-core locations, isochrones and LGM extent) for each of the 3,000 simulations. Each dot represents a simulation, and the best simulation (with the highest global score S) is marked in red. The colorbar represents the score S and the x-axis represents the simulation number.

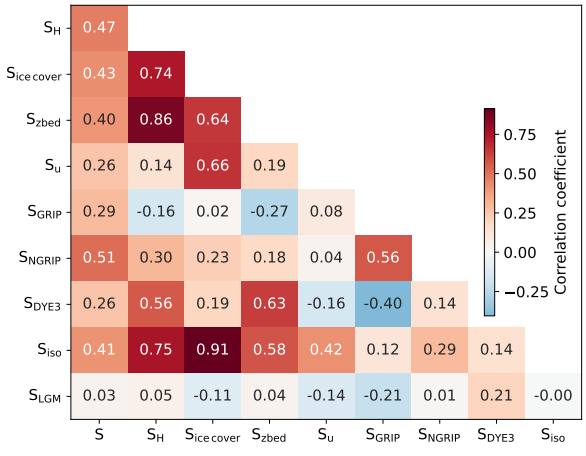

Figure 10. Correlation coefficients of each pair of scores.

https://doi.org/10.5194/egusphere-2026-3331
Preprint. Discussion started: 25 June 2026

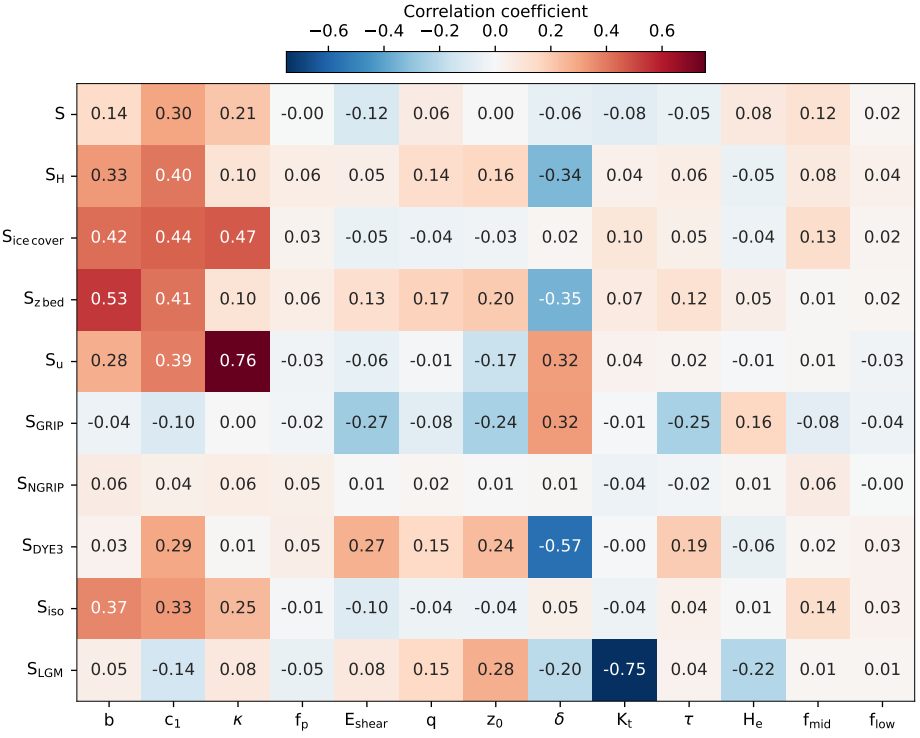

Figure 11. Correlation between global score S, individual scores S_i, and each of the parameters perturbed in the ensemble.

velocities (S_u). An accurate surface velocity field requires an ice extent that closely matches observations, which in turn is strongly controlled by ocean sensitivity. In ensemble members where the ice margin extends beyond its present-day position, artificially high velocities are generated in those marginal areas – regions that should be ice-free and therefore have zero velocity. In addition, ocean sensitivity governs the presence of ice shelves, which in turn modulate inland ice dynamics through buttressing effects. While the strong influence of ocean sensitivity on colder climates has been demonstrated in previous studies (Tabone et al., 2018; Gutiérrez-González et al., 2026a), the present results further reveal that its effects extend to and are still imprinted on the present-day configuration of the ice sheet when simulating from the LGM.

The parameters associated with basal dynamics (q, z_0, and δ) as well as the ice rheology parameter (E_{shear}) affect the evaluated scores differently. The ice thickness score (S_{H}), and consequently the bedrock-elevation score ($S_{\text{z bed}}$) – which is largely controlled by the ice load above – together with S_{LGM} and $S_{\text{DYE-3}}$, exhibit a negative correlation with δ and a positive correlation with z_0, q, and E_{shear}. The influence of E_{shear} is however generally weak across the evaluated scores, only reaching a significant value of almost 0.3 for $S_{\text{DYE-3}}$ and S_{GRIP}. An increase in the parameter δ, defined as a fraction of the overburden pressure, increases the effective pressure N_{eff}, thereby enhancing basal friction (Eqs. 4 and 2). In contrast, z_0 represents the bedrock depth threshold below which basal friction begins to decay, accounting for enhanced sliding in topographically depressed areas; consequently, higher values of z_0 reduce basal friction in general terms (Eqs. 3 and 2). Similarly, higher values of

https://doi.org/10.5194/egusphere-2026-3331
Preprint. Discussion started: 25 June 2026

the friction-law exponent q also reduce basal friction (Eq. 1), while increasing E_{shear} enhances deformation in shear-dominated flow regimes. These results indicate that accurately reproducing the present-day ice thickness, the LGM margin position, and the surface elevation at DYE-3 requires a flow regime characterized by enhanced sliding and deformation (inside the parameter range of study). In the case of DYE-3, this can be attributed to its more marginal location relative to the other ice core sites.

The opposite behavior is observed for the present-day ice surface velocity score (S_{u}) and the surface elevation evolution at GRIP (S_{GRIP}), both of which favor parameter combinations yielding slower ice dynamics and reduced deformation. This is consistent with the central location of the GRIP ice core, where deformation-driven flow is limited. Regarding surface velocities, this reflects the fact that simulated velocities are generally slightly overestimated across the ensemble.

The choice of basal and rheological parameters therefore exerts considerable influence on the representation of the GrIS throughout the deglaciation, in a way that does not point to a single optimal configuration. Rather, trade-offs are possible between combinations of parameter values depending on which regions or observational targets are prioritized in the model evaluation.

The calving parameter κ_t has a limited impact on most scores, with the notable exception of the LGM ice mask score (S_{LGM}), for which the negative correlation is substantial (-0.75). This indicates, as expected, that an adequate representation of calving has little bearing on the present-day state of the GrIS – since ice shelves and ice-ocean contact zones are far less extensive today than they were in the past – but is critical for reproducing the past ice-sheet extent. This behavior was already apparent in Figs. 9 and 10, where S_{LGM} appeared largely independent of the remaining scores and showed no clear relationship with the global score. We therefore conclude that, when aiming to reproduce a full GrIS deglaciation, the calving parameter should be calibrated against the known LGM ice extent.

The influence of solid Earth parameters on deglaciation performance is also ambiguous, as they correlate positively or negatively depending on the individual score considered. As described in Sect. 2, the simulations employ an ELRA model in which the lithosphere is treated as an elastic plate of uniform thickness H_e, and the asthenosphere is viscous with a relaxation time τ. H_e shows a significant correlation only with S_{LGM}, and this correlation is negative, suggesting that an accurate representation of the LGM extent requires a relatively thin lithosphere. τ, in contrast, shows a significant correlation only with S_{GRIP}, favoring short relaxation times and therefore a faster glacial isostatic adjustment, which seems to be necessary to accurately capture the surface elevation changes recorded at GRIP. However, these results should be interpreted with caution given the simplicity of the ELRA approach.

Finally, from the parameters controlling basal friction in the NEGIS, only f_{mid} has an effect on S, and surprisingly, none of them has a significant linear impact on S_{NGRIP}. Indeed, S_{NGRIP} does not exhibit a clear linear dependency on any of the ensemble parameters.

3.3.1 Emulator-based sensitivity analysis

To explore the sensitivity of the global score S to the ensemble parameters, we developed an emulator model based on the eXtreme Gradient Boosting (XGBoost) algorithm (Chen and Guestrin, 2016). The model uses the specific parameter combinations of each simulation as input features to predict the resulting performance score S. The dataset was partitioned into a training

https://doi.org/10.5194/egusphere-2026-3331
Preprint. Discussion started: 25 June 2026

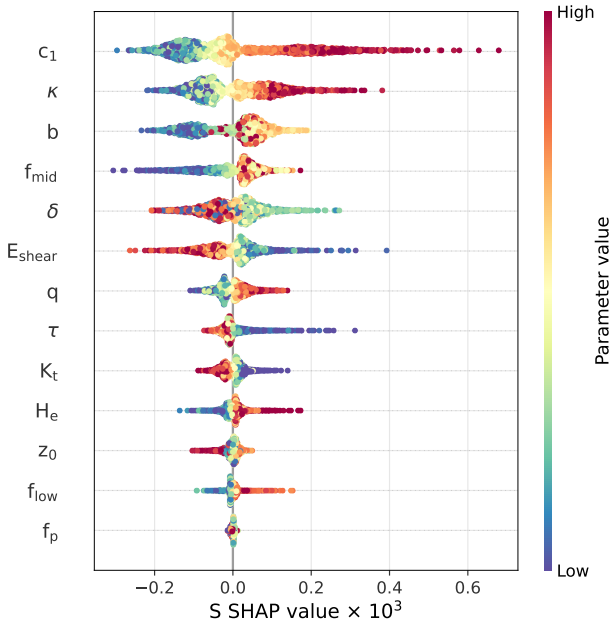

Figure 12. SHAP values of the global score S for each of the parameters perturbed in the ensemble (Table 2), calculated with a XGBRegressor model with a determination coefficient R^2=0.39 in the validation test.

set (90%) and an independent testing set (10%). Hyperparameter optimization was conducted via a 5-fold cross-validated grid search on the training partition. To mitigate overfitting within this high-dimensional parameter space, we enforced stringent regularization constraints, including a high penalty (λ term in Chen and Guestrin, 2016) and a restricted maximum tree depth.

The optimized emulator achieved a cross-validated determination coefficient (R^2) of 0.34. Following the selection of optimal hyperparameters, the model was retrained on the full training set, yielding an R^2 of 0.60. The final model performance was evaluated on the independent testing set, resulting in an R^2 of 0.43. While these values indicate that the emulator accounts for a moderate fraction of the total variance, such performance is expected given the extreme dimensionality reduction involved in emulating a complex, non-linear system like an ice sheet. However, the close agreement between the cross-validation and testing metrics confirms that the model successfully generalizes the primary physical sensitivities without overfitting to the training data.

Thereafter, we performed an interpretability analysis to attribute parameter influence to the global score S within the fraction of variance captured by the XGBoost model. For this purpose, we employed SHAP (SHapley Additive exPlanations) framework, based on the Shapley values developed in the game-theory approach that quantifies the marginal contribution of each parameter to the predicted score (Shapley, 1953). This approach allows for the quantification of the relative importance of parameters in the global performance of the simulations (Lundberg et al., 2020; Kellner et al., 2022). Fig. 12 presents a summary of these SHAP values (all the SHAP values are shown against the different parameter values in Fig. S1 of the Supplementary Material), illustrating both the hierarchy of parameter importance and the directionality of their impact. Within this plot, the

https://doi.org/10.5194/egusphere-2026-3331
Preprint. Discussion started: 25 June 2026

vertical position indicates the relative importance of the variable, while the horizontal axis represents the magnitude and sign of its influence on S. For instance, c_1 is the parameter with the greatest impact on S: low values of c_1 are associated with lower scores, whereas high values (shown in red) yield SHAP values in the range 0.2–0.7×10^{-3}, indicating that they can lead to moderate-to-high scores. In other words, low values of c_1 consistently degrade S, while high values either leave it unchanged or improve it, with a marked improvement in score for $c_1 > 27.5\,\mathrm{W\,m^{-2}}$. As indicated by Eq.6, this suggests that the prescribed precipitation (Badgeley et al., 2020) and temperature (Buizert et al., 2018) forcings for this setting need an upward adjustment to surface melting to achieve satisfactory model performance.

The SHAP value analysis is complementary to the correlation matrix presented in Fig.11 in several ways: (1) it provides an independent method that strengthens conclusions shared by both approaches, and (2) it captures non-linear dependencies between S and the different parameters, which are not reflected in the correlation matrix.

As revealed by the correlation matrix, the parameters with the greatest influence on S are c_1, b, and κ, with c_1 showing the highest potential to improve model performance. Notably, however, the variable most detrimental to overall performance is f_{mid}, which does not rank prominently in the correlation matrix. This variable exhibits a threshold behavior: when f_{mid} takes low values within the explored range ($f_{\mathrm{mid}} < 0.45$), basal friction in the NEGIS central stream is reduced excessively, allowing an unrealistically large advance of the ice margin in that region at the present day.

Additionally, the asthenospheric relaxation time τ also exhibits a significant non-linear impact: below a threshold value, it contributes positively to S, but for $\tau > 1300\,\mathrm{yr}$ its influence becomes neutral or even detrimental. A similar behavior is observed for E_{shear}, whose positive influence diminishes for values above 1.3. Likewise, f_p showed no clear linear correlation with S, yet the SHAP analysis reveals that values above 1.1 can degrade performance, suggesting a sensitivity that the correlation matrix alone could not capture. Overall, the SHAP results are consistent with the preceding correlation analysis, while providing a more thorough characterisation of parameter influence, particularly for parameters exhibiting threshold-dependent behaviour.

4 Discussion

4.1 GrIS deglaciation performance: strengths and misfits

In this study, we have assessed the ability of the last deglaciation ensemble of Tabone et al. (2024) to reproduce several observational constraints from both the past and present states of the GrIS. From this ensemble, we identify a best-fit simulation yielding an LGM state almost reaching the continental-shelf break along the margin, followed by a rapid retreat onset at approximately 15 kyr BP, a slowdown — without a complete halt — of deglaciation during the Younger Dryas, and a minimum extent reached around 5 kyr ago, approximately 3 kyr after the HTM. Thereafter, cooling temperatures drive a gradual readvance of the ice sheet toward a present-day configuration consistent with modern observations.

Model simulations of the GrIS deglaciation have generally struggled to represent both the LGM and the present-day ice-sheet extension (Fig. 13). PaleoMIST (Gowan et al., 2021) provides the closest match to the present-day grounded area, notably for the Holocene; however, it substantially underestimates the LGM extent, falling well below the observational uncertainty range before the onset of retreat. Leger et al. (2025) present an ensemble of simulations, of which we show one of their five

https://doi.org/10.5194/egusphere-2026-3331
Preprint. Discussion started: 25 June 2026

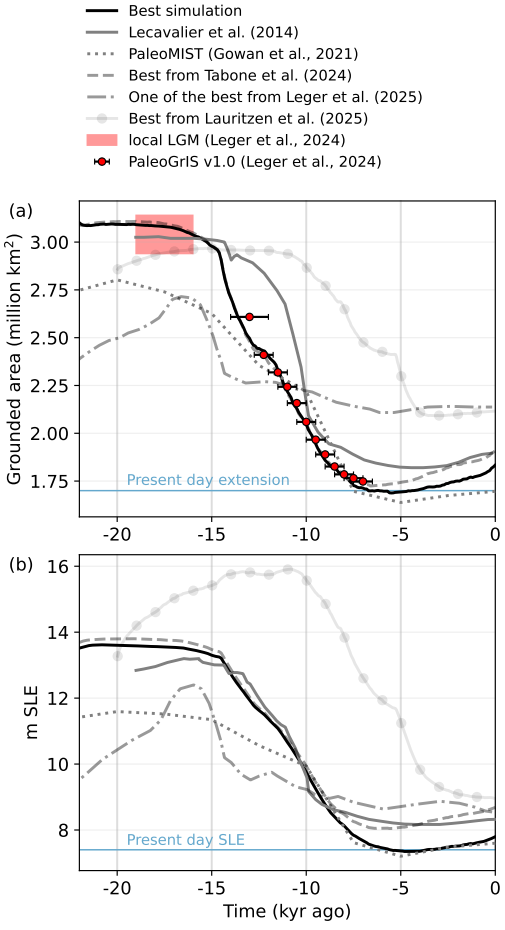

Figure 13. Comparison between different reconstructions of the GrIS for the last deglaciation (black and gray lines), margin reconstruction calculated from PaleoGrIS v1.0 isochrones (red dots, Leger et al., 2024) and present-day observations (Morlighem et al., 2017). a) Grounded area and b) volume in sea level equivalent.

best-performing members. While other members of their ensemble fall within the uncertainty bounds of the LGM maximum extent mask, none retreats far enough to reach a present-day configuration consistent with observations. Similarly, Lauritzen et al. (2024) produce an LGM extent in good agreement with observations, but the ice sheet fails to retreat to its modern margin.

In this sense, Lecavalier et al. (2014) can be considered the most skillful among the previously published reconstructions, as it falls within the plausible range of LGM extent and achieves a present-day state with a root-mean-square error in ice thickness of 214.1 m and a grounded area overestimation of approximately 12% — a notable achievement given the use of the Shallow Ice Approximation on a coarse grid (20 km). However, in light of the subsequent PaleoGrIS v1.0 isochrone reconstruction, this simulation exhibits a slightly delayed onset of ice loss relative to the observational record. Both the best simulation of Tabone et al. (2024) and the best simulation found here from the same ensemble closely track the observational uncertainty bounds in

https://doi.org/10.5194/egusphere-2026-3331
Preprint. Discussion started: 25 June 2026

grounded area throughout the last deglaciation. The primary distinction lies in their present-day states: as the study by Tabone et al. (2024) was focused on capturing the NGRIP-elevation evolution through a correct representation of the NEGIS, its best simulation converges on a higher present-day ice volume, with a root-mean-square error in ice thickness of 258 m. As a result, it tends to perform better in terms of surface velocities across the whole domain and ice thickness in the northeast sector, but less well across the remainder of the GrIS (see Fig. 2 in the Supplement). In both cases, the model struggles to reproduce the correct ice thickness along the southeast and southwest margin, due to the presence of narrow fjords that are not resolved at 8 km grid resolution. This is a well-known limitation of GrIS modelling at this and lower resolutions (Stone et al., 2010; Robinson et al., 2012; Born and Nisancioglu, 2012; Tabone et al., 2018; Höning et al., 2023; Gutiérrez-González et al., 2026a); however, an 8 km resolution remains necessary to make transient ensemble simulations spanning 22 kyr computationally feasible.

In terms of SLE (Fig. 13b), both the best simulation of Tabone et al. (2024) and the one presented here follow a trajectory closely aligned with that of Lecavalier et al. (2014) until approximately 9 kyr BP, after which Lecavalier et al. (2014) fails to retreat sufficiently in certain regions, leading to a divergence toward higher ice volumes relative to the present day.

Although our best simulation still exhibits discrepancies with observations for the present-day state (Sect. 3.2.2), it provides the best representation among those simulations capable of reproducing a plausible LGM and a correct deglaciation timing. The main caveat of this simulation— and of the ensemble in general — as well as one primary target for future improvement, is its inability to capture the reconstructed elevation change at Camp Century (Fig. 4). This is a common limitation among ice-sheet models (Lecavalier et al., 2014; Leger et al., 2025; Gowan et al., 2021). The only study that successfully reproduces this feature is Lauritzen et al. (2024), under the premise that correctly capturing it requires extending the simulated domain to allow for a large ice shelf in Baffin Bay, connected to the Innuitian Ice Sheet. Such a configuration generates a buttressing effect that sustains greater ice thicknesses before deglacial retreat, followed by a substantial thinning upon ice shelf loss. A further consideration is that the reconstructed elevation changes used herein are based on Vinther et al. (2009). A later study by Lecavalier et al. (2017), however, suggested that ice thickness changes at Camp Century may have been even larger than previously estimated — in which case even the simulation of Lauritzen et al. (2024) might underestimate the thinning. Regardless, the interpretation of Lauritzen et al. (2024) is further supported by comparing the simulated grounding line here and the target LGM mask discussed in Sect. 3.2. Agreement is broadly found along most of the coastline, but breaks down in the vicinity of Ellesmere Island, the region where a more extensive connection with the northern Canadian ice complex would be expected. Since this study does not implement the extended domain suggested by Lauritzen et al. (2024), this remains an avenue for future improvement; consequently, the Camp Century elevation score was excluded from the model evaluation.

Beyond ice dynamics, several simplifications related to the representation of the solid Earth also merit consideration. ELRA assumes a constant relaxation time, which in reality depends both on the horizontal extent of the load and on the laterally variable properties of the solid Earth. Recent work has demonstrated important differences in viscosity and lithospheric thickness between eastern and western Greenland (Bagge et al., 2021; Steffen et al., 2018). This lateral variability has been shown to greatly influence simulated present-day uplift rates (Milne et al., 2018), an additional constraint that was not incorporated here given the limitations of the model setup.

https://doi.org/10.5194/egusphere-2026-3331
Preprint. Discussion started: 25 June 2026

A further simplification concerns the gravitational and rotational feedbacks in the GIA response, which are excluded from the present model setup. Accounting for these feedbacks interactively would require a full Northern Hemisphere domain, which is not only a limitation of the model itself but also of the current regional setup. As a result, only barystatic sea-level variations are considered, and spatially heterogeneous sea-surface elevation is neglected. Since the latter is important for accurate RSL computation, observational RSL constraints — available for some locations during the last deglaciation (Gowan, 2023) — were not incorporated into the evaluation.

Finally, our results demonstrate that the performance of the simulations in reproducing deglacial observables is primarily driven by the specific ice-sheet sensitivity to climate forcing. The selected forcings (Buizert et al., 2018; Badgeley et al., 2020) appear to effectively capture the reconstructed temperature and precipitation patterns characteristic of the deglaciation. Driving the ice sheet with these climatic fields serves as a robust approach to reduce the degrees of freedom within the system, effectively constraining the ice-sheet evolution to the observational record. However, this one-way forcing implies that the impact of ice-sheet evolution on the large-scale climate is ignored. A clear next step would be to address the problem with fully coupled simulations in future work.

4.2 Global-sea-level contribution during the LGM and after the HTM

We now show the contributions to global mean sea-level change ($\Delta\mathrm{GMSL}$) during the LGM and the HTM from the best-fit simulation in the context of the broader ensemble (Fig. 14b and d) and previous studies (Fig. 14a and c). As shown in Fig. 14a, there is considerable uncertainty in the $\Delta\mathrm{GMSL}$ during the LGM, with estimates ranging from -2 m (Clark and Mix, 2002) to -6 m (Leger et al., 2025) (i.e., LGM sea-level equivalent volumes 2-6 m larger than today). Furthermore, some studies distinguish between the sea-level contribution computed over the LGM and that over the local LGM, the latter corresponding to the period of maximum ice extent and therefore most directly comparable to geological observations. In our simulations, as shown in Figs. 2 and 13, no significant volume increase is found between the LGM period and the maximum ice volume, and we therefore report the $\Delta\mathrm{GMSL}$ for the LGM as the mean over the 19–16 kyr BP interval. Our best-fit simulation yields a GrIS contribution to GMSL reduction of 5.75 m, with the 68 % cumulative frequency range spanning from 3.93 to 6.31 m, calculated by ranking simulations according to their scores. This value falls within the range reported in the literature, although toward the upper end. However, models producing $\Delta\mathrm{GMSL}$ contributions below 4 m (in absolute value) generally exhibit sparse or absent ice shelves and a more retreated margin than our best-fit simulation, particularly in the northeast (Clark and Mix, 2002; Huybrechts, 2002), a region where subsequent work has shown the margin to have been more advanced than previously thought (Arndt et al., 2017). In some of these studies, the connection with Ellesmere Island is narrower (Bradley et al., 2018), while in others the lower contribution to sea-level reduction is attributable to the fact that it is computed relative to a final deglaciated state that does not reach the present-day extent (Quiquet et al., 2021), even when the simulated LGM extent is otherwise adequate.

Regarding the minimal extension of the GrIS, it was reached after the HTM, which exhibits summer temperatures around Greenland +2.1°C higher than present-day values in our forcing. Following this warming, our best-fit simulation generates a GMSL contribution of 0.45 m, with an uncertainty range spanning from 0.43 to 1.18 m. This range is broadly consistent

https://doi.org/10.5194/egusphere-2026-3331
Preprint. Discussion started: 25 June 2026

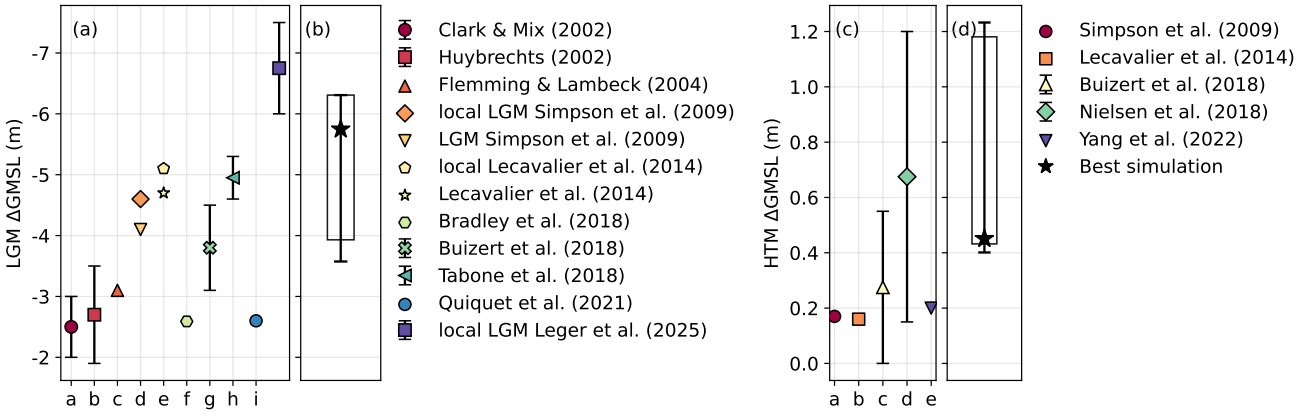

Figure 14. GrIS contribution to global sea-level changes at the (a) LGM and (c) HTM compared across different studies. (b) and (d) GrIS contribution to global sea-level changes from our ensemble. The stars indicate the sea-level contribution of the best simulation (LGM: -5.75 m; HTM: 0.45 m). Boxes and whiskers denote the 68% and 95% cumulative frequency ranges, respectively. Each of these anomalies is calculated with respect to the present-day state of each simulation.

with previous modelling studies, though it sits towards the upper end of published estimates. Simpson et al. (2009) simulated a margin retreat of 60–100 km in the southwest and approximately 80 km in the northeast, while Lecavalier et al. (2014) obtained more modest retreats of 20–60 km in the southwest. Tarasov and Peltier (2002) simulated retreats of 60–160 km in the southwest, and Nielsen et al. (2018) estimated retreats of 30–60 km in the southwest and 10–40 km in the north. Fleming and Lambeck (2004) have a retreat of approximately 40 km behind the present-day margin in the west, and Leger et al. (2025) showed retreats of up to ∼100 km south of 68° N, with little to no retreat in the northern sectors. The southwestern retreat simulated here — reaching up to 100 km in the Kangerlussuaq region — thus falls at the upper bound of this range.

How far the GrIS retreated during the Holocene is challenging to quantify. While it is known that it retreated behind its current margin, the precise magnitude of this retreat along the coast cannot be completely determined, as its subsequent re-advance prevents the observation of any formerly deposited moraines (Young and Briner, 2015; Funder et al., 2011) and we only have cosmogenic dating of recently deglaciated bedrock and indirect measurements based on lake sediments and marine fauna. It is known, however, that this minimum extent was reached between approximately 6 and 4 kyr ago according to Briner et al. (2020), and likely after ∼5 kyr ago (Young et al., 2021), which is consistent with our simulation timing. Observational records indicate that the most substantial changes occurred in the southwest, specifically in the Kangerlussuaq region, where different indirect estimates range between 2 and 26 km (Willemse et al., 2003; Young and Briner, 2015; Lesnek et al., 2020; Young et al., 2021). Significant retreat is also documented in Northeast Greenland, that retreated 30 to 40 km behind its present-day extent (Larsen et al., 2020, 2022) and even more in areas with deep fjords like the 79° North Glacier, that retreated at least 70 km (Bennike and Weidick, 2001).

https://doi.org/10.5194/egusphere-2026-3331
Preprint. Discussion started: 25 June 2026

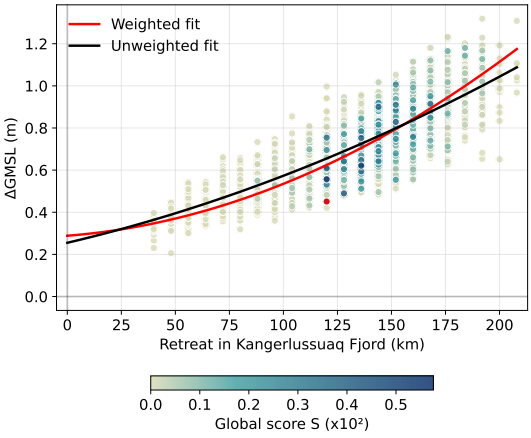

Figure 15. Relationship between ice-front retreat in Kangerlussuaq Fjord and ΔGMSL contribution. Individual simulations are shown as circles, with colors representing their respective global scores. The red curve denotes a weighted second-order polynomial fit, the coefficients of which are summarized in the Supplement. Uncertainties in the coefficients correspond to the standard error derived from the covariance matrix.

The southwestern retreat in our simulation, while spatially consistent with observations, may therefore be overestimated, particularly in the Kangerlussuaq region, where simulated retreat reaches up to 100 km at some locations, well beyond the reconstructed range of 2–26 km mentioned above. Among studies simulating past GrIS evolution, only Briner et al. (2020) achieves a good agreement with reconstructions in the southwest, although their simulation was restricted to this sector. This discrepancy may partly reflect insufficient precipitation in this region during the HTM, which is known to have played a critical role in limiting the ice-margin retreat in response to temperature forcing (Thomas et al., 2016) or an overestimation of regional warming. In this regard, Briner et al. (2020) use Badgeley et al. (2020) as forcing for both precipitation and temperature, whereas we prescribe temperatures from Buizert et al. (2018), which exhibits a slightly stronger HTM warming and could therefore account for the excessive retreat simulated here. Nevertheless, this remains a common limitation among ice-sheet models simulating the GrIS through the last deglaciation.

Furthermore, Lecavalier et al. (2014) demonstrated that a sufficiently large retreat and consequent readvance of the GrIS is required to reconcile RSL observations from west Greenland, suggesting that the precise magnitude of HTM retreat could be larger than what indirect observations show. Taken together, these considerations indicate that the minimum extent of the GrIS during the Holocene remains an open question, and that improved representation of regional temperature and precipitation patterns and ice–climate interactions will be essential for progress.

The Kangerlussuaq region exhibits the largest differences with respect to the present-day ice sheet configuration, both in terms of maximum retreat distance and in the areal extent of the retreat, which is more spatially widespread than the deeper but more confined retreat observed in the northeast. As a consequence, this region also represents the dominant source of GrIS contribution to GMSL rise during the HTM. Furthermore, as discussed above, it is characterised by the largest model–observation

https://doi.org/10.5194/egusphere-2026-3331
Preprint. Discussion started: 25 June 2026

discrepancies across modelling studies, including our own simulation. The retreat of Kangerlussuaq glacier may serve as a proxy for the total GrIS sea level contribution during the HTM. This is consistent with Briner et al. (2020), who showed that mass loss in the west–southwest domain correlates strongly with the entire ice sheet, and with Keisling et al. (2026), who identifies southwest Greenland as the primary region contributing to the first meters of sea-level rise across diverse warming scenarios. To explore this relationship, we evaluate the correlation between retreat and $\Delta\mathrm{GMSL}$ using both weighted (by simulation score) and unweighted second-order polynomial fits (Fig.15). Both fits yield a strong correlation between simulated retreat and ensemble GMSL contribution; however, the coefficients of both fits carry large uncertainties, and all simulations achieving high performance scores consistently exhibit retreats exceeding 100 km. This clustering suggests that more robust constraints on Kangerlussuaq retreat — derived from improved modelling and palaeoglaciological data — could provide a critical observational target for narrowing uncertainties in GrIS sea level estimates during the Holocene minimum.

5 Conclusions

In this study, we have analyzed the 3,000-simulation ensemble of Tabone et al. (2024) to identify a best-fit simulation of the GrIS evolution through the last deglaciation: one that simultaneously satisfies observational constraints on the LGM margin extent, the timing and pattern of margin retreat, ice-surface elevation changes at ice core sites, and the present-day ice sheet configuration. In this way we provide a best-fit simulation that improves upon previous reconstructions when considering all constraints together, even if individual metrics are not always individually better. This simulation is available for use as boundary conditions in coupled climate models, GIA models or as an estimate of the GrIS contribution to global mean sea level change through the last deglaciation.

This best-fit simulation yields a GrIS contribution to GMSL of -5.75 m SLE at the LGM, with an ensemble uncertainty range of -3.93 to -6.31 m SLE. During the HTM — a period during which Greenland summer temperatures exceeded present-day values — the simulated contribution reaches 0.45 m SLE, with an ensemble uncertainty range of 0.45 to 1.18 m SLE. These values are in the upper-middle range of previous estimates.

From the analysis of the ensemble performance of the different scores, we highlight the following findings. The sensitivity of the ice sheet to atmospheric and oceanic climate forcing is the primary control on the last deglaciation performance. The calving parameterization, in contrast, exerts its influence almost exclusively on the LGM state, which is itself largely controlled by calving processes. This implies that, when seeking to reproduce glacial–interglacial transitions of the GrIS, calving laws and associated parameters should be calibrated with particular attention to the representation of the LGM state, for which several observational records are available. Furthermore, reducing uncertainties in margin-position observations in the southwest (the Kangerlussuaq region), and improving the ability of models to match those constraints, appears critical for adequately estimating the GrIS contribution to sea level following the HTM. Finally, although a horizontal resolution of 8 km does not resolve all relevant present-day processes — such as flow through narrow fjords — it proves sufficient for an adequate representation of the broad deglaciation history of the GrIS, offering a practical balance between computational cost and model performance.

https://doi.org/10.5194/egusphere-2026-3331
Preprint. Discussion started: 25 June 2026

Despite these advances, significant scope for improvement remains. In particular, future work should focus on extending the simulated domain to incorporate the connection with the LIS, which appears necessary to reproduce elevation changes at Camp Century and the full LGM extent near Ellesmere Island. More broadly, fully coupled ice sheet–climate simulations and improved representations of GIA will be essential to better reproduce the processes governing deglacial ice-sheet evolution, and would further enable the incorporation of additional observational constraints — such as RSL records and bedrock uplift rates — that have not been considered in the present study.

Code and data availability. The data used in the validation process of the simulations can be found at https://github.com/fesmc/FesmData (last access: 8 June 2026). The scripts for the processing of the simulations, the calculation of the scores, and the generation of the figures included in the present work, as well as the datasets with the individual scores and the 1D fields of the ensemble simulations, can be found at https://github.com/luciagutierrezg/GrIS_deglaciation_yelmox (last access: 8 June 2026). The best simulation file and video can be found on Zenodo (https://zenodo.org/records/20544171, Gutiérrez-González et al., 2026b).

Author contributions. L.G.G. developed the analysis and wrote the paper. IT provided the ensemble simulations and contributed with the revision of the manuscript. All other authors contributed to the analysis of the results and the revision of the manuscript.

Competing interests. M.M. is member of the editorial board of Climate of the Past.

Acknowledgements. L.G.G. is funded by the Comunidad de Madrid (grant no. CT15/23). A.R. and B.G. received funding from the European Union (ERC, FORCLIMA, 101044247). J.A.S. received funding from Spanish Ministry of Science and Innovation (project CCRYTICAS, grant no. PID2022-142800OB-I00). This research has been supported by the Spanish Ministry of Science and Innovation under the project CREEP (Improving the representation of critical features leading to deep uncertainty in ice-sheet projections, grant no. PID2024-156476OB-I00). This is ClimTip contribution #171; the ClimTip project has received funding from the European Union's Horizon Europe research and innovation programme under grant agreement No. 101137601. This research has been supported by European Union funding (Horizon Europe, P2F, 101184070).

https://doi.org/10.5194/egusphere-2026-3331
Preprint. Discussion started: 25 June 2026

References

Arndt, J. E., Jokat, W., and Dorschel, B.: The last glaciation and deglaciation of the Northeast Greenland continental shelf revealed by hydro-acoustic data, Quaternary Science Reviews, 160, 45–56, https://doi.org/https://doi.org/10.1016/j.quascirev.2017.01.018, 2017.

Badgeley, J. A., Steig, E. J., Hakim, G. J., and Fudge, T. J.: Greenland temperature and precipitation over the last 20,000 years using data assimilation, Climate of the Past, 16, 1325–1346, https://doi.org/10.5194/cp-16-1325-2020, 2020.

Bagge, M., Klemann, V., Steinberger, B., Latinović, M., and Thomas, M.: Glacial-Isostatic Adjustment Models Using Geodynamically Constrained 3D Earth Structures, Geochemistry, Geophysics, Geosystems, 22, e2021GC009 853, https://doi.org/10.1029/2021GC009853, 2021.

Bennike, O. and Weidick, A.: Late Quaternary history around Nioghalvfjerdsfjorden and Jøkelbugten, North-East Greenland, Boreas, 30, 205–227, https://doi.org/10.1111/j.1502-3885.2001.tb01018.x, 2001.

Blasco, J., Tabone, I., Moreno-Parada, D., Robinson, A., Alvarez-Solas, J., Pattyn, F., and Montoya, M.: Antarctic tipping points triggered by the mid-Pliocene warm climate, Climate of the Past, 20, 1919–1938, https://doi.org/10.5194/cp-20-1919-2024, 2024.

Born, A. and Nisancioglu, K. H.: Melting of Northern Greenland during the last interglaciation, The Cryosphere, 6, 1239–1250, https://doi.org/10.5194/tc-6-1239-2012, 2012.

Box, J. E.: Greenland Ice Sheet Mass Balance Reconstruction. Part II: Surface Mass Balance (1840–2010), Journal of Climate, 26, 6974–6989, https://doi.org/10.1175/JCLI-D-12-00518.1, 2013.

Bradley, S. L., Reerink, T. J., van de Wal, R. S. W., and Helsen, M. M.: Simulation of the Greenland Ice Sheet over two glacial–interglacial cycles: investigating a sub-ice-shelf melt parameterization and relative sea level forcing in an ice-sheet–ice-shelf model, Climate of the Past, 14, 619–635, https://doi.org/10.5194/cp-14-619-2018, 2018.

Briner, J. P., McKay, N. P., Axford, Y., Bennike, O., Bradley, R. S., de Vernal, A., Fisher, D., Francus, P., Fréchette, B., Gajewski, K., Jennings, A., Kaufman, D. S., Miller, G., Rouston, C., and Wagner, B.: Holocene climate change in Arctic Canada and Greenland, Quaternary Science Reviews, 147, 340–364, https://doi.org/https://doi.org/10.1016/j.quascirev.2016.02.010, special Issue: PAST Gateways (Palaeo-Arctic Spatial and Temporal Gateways), 2016.

Briner, J. P., Cuzzone, J. K., Badgeley, J. A., Young, N. E., Steig, E. J., Morlighem, M., Schlegel, N.-J., Hakim, G. J., and Schaefer, J. M.: Rate of mass loss from the Greenland Ice Sheet will exceed Holocene values this century, Nature, 586, 70–74, https://doi.org/10.1038/s41586-020-2742-6, 2020.

Bueler, E. and van Pelt, W.: Mass-conserving subglacial hydrology in the Parallel Ice Sheet Model version 0.6, Geoscientific Model Development, 8, 1613–1635, 2015.

Buizert, C., Keisling, B. A., Box, J. E., He, F., Carlson, A. E., Sinclair, G., and DeConto, R. M.: Greenland-wide seasonal temperatures during the last deglaciation, Geophysical Research Letters, 45, 1905–1914, https://doi.org/10.1002/2017GL075601, 2018.

Chen, T. and Guestrin, C.: XGBoost: A Scalable Tree Boosting System, in: Proceedings of the 22nd ACM SIGKDD International Conference on Knowledge Discovery and Data Mining, pp. 785–794, ACM, https://doi.org/10.1145/2939672.2939785, 2016.

Clark, P. U. and Mix, A. C.: Ice sheets and sea level of the Last Glacial Maximum, Quaternary Science Reviews, 21, 1–7, https://doi.org/10.1016/S0277-3791(01)00118-4, 2002.

Evans, J., Ó Cofaigh, C., Dowdeswell, J. A., and Wadhams, P.: Marine geophysical evidence for former expansion and flow of the Greenland Ice Sheet across the north-east Greenland continental shelf, Journal of Quaternary Science: Published for the Quaternary Research Association, 24, 279–293, 2009.

https://doi.org/10.5194/egusphere-2026-3331
Preprint. Discussion started: 25 June 2026

Fleming, K. and Lambeck, K.: Constraints on the Greenland Ice Sheet since the Last Glacial Maximum from sea-level observations and glacial-rebound models, Quaternary Science Reviews, 23, 1053–1077, https://doi.org/10.1016/j.quascirev.2003.11.001, 2004.

Funder, S., Kjeldsen, K. K., Kjær, K. H., and Ó Cofaigh, C.: The Greenland Ice Sheet During the Past 300,000 Years: A Review, in: Quaternary Glaciations - Extent and Chronology: A Closer Look, vol. 15 of *Developments in Quaternary Science*, pp. 699–713, Elsevier, https://doi.org/10.1016/B978-0-444-53447-7.00050-7, 2011.

Gowan, E. J.: Paleo sea-level indicators and proxies from Greenland in the GAPSLIP database and comparison with modelled sea level from the PaleoMIST ice-sheet reconstruction, GEUS Bulletin, 53, https://doi.org/10.34194/geusb.v53.8355, 2023.

Gowan, E. J., Zhang, X., Khosravi, S., Rovere, A., Stocchi, P., Hughes, A. L. C., Gyllencreutz, R., Mangerud, J., Svendsen, J. I., and Lohmann, G.: A new global ice sheet reconstruction for the past 80 000 years, Nature Communications, 12, 1199, https://doi.org/10.1038/s41467-021-21469-w, 2021.

Gutiérrez-González, L., Robinson, A., Alvarez-Solas, J., Tabone, I., Swierczek-Jereczek, J., Moreno-Parada, D., and Montoya, M.: Hysteresis of the Greenland ice sheet from the Last Glacial Maximum to the future, The Cryosphere, 20, 1139–1162, https://doi.org/10.5194/tc-20-1139-2026, 2026a.

Gutiérrez-González, L., Tabone, I., Robinson, A., Alvarez-Solas, J., Swierczek-Jereczek, J., Grusdt, B., and Montoya, M.: Ensemble reconstruction of the Greenland Ice Sheet evolution through the last deglaciation: video and dataset of the best simulation, Zenodo, https://doi.org/10.5281/zenodo.20544171, 2026b.

He, F., Shakun, J. D., Clark, P. U., Carlson, A. E., Liu, Z., Otto-Bliesner, B. L., and Kutzbach, J. E.: Northern Hemisphere forcing of Southern Hemisphere climate during the last deglaciation, Nature, 494, 81–85, https://doi.org/10.1038/nature11822, 2013.

Höning, D., Willeit, M., Calov, R., Klemann, V., Bagge, M., and Ganopolski, A.: Multistability and transient response of the Greenland ice sheet to anthropogenic CO2 emissions, Geophysical Research Letters, 50, e2022GL101 827, 2023.

Huybrechts, P.: Sea-level changes at the LGM from ice-dynamic reconstructions of the Greenland and Antarctic ice sheets during the glacial cycles, Quaternary Science Reviews, 21, 203–231, https://doi.org/10.1016/S0277-3791(01)00082-8, 2002.

IPCC: Climate Change 2021: The Physical Science Basis, IPCC Sixth Assessment Report, Cambridge University Press, Cambridge, United Kingdom and New York, NY, USA, https://doi.org/10.1017/9781009157896, 2021.

Joughin, I., SMITH, B. E., and HOWAT, I. M.: A complete map of Greenland ice velocity derived from satellite data collected over 20 years, Journal of Glaciology, 64, 1–11, https://doi.org/10.1017/jog.2017.73, 2018.

Joughin, I., Smith, B. E., and Schoof, C. G.: Regularized Coulomb friction laws for ice sheet sliding: Application to Pine Island Glacier, Antarctica, Geophysical research letters, 46, 4764–4771, 2019.

Keisling, B. A., Schaefer, J. M., DeConto, R. M., Briner, J. P., Young, N. E., Walcott-George, C. K., Winckler, G., Balter-Kennedy, A., and Anandakrishnan, S.: An ice-sheet modelling framework to determine vulnerable regions of the Greenland Ice Sheet in the past, The Cryosphere, 20, 2961–2976, https://doi.org/10.5194/tc-20-2961-2026, 2026.

Kellner, L., Stender, M., von Bock und Polach, F., and Ehlers, S.: Predicting compressive strength and behavior of ice and analyzing feature importance with explainable machine learning models, Ocean Engineering, 255, 111 396, https://doi.org/10.1016/j.oceaneng.2022.111396, 2022.

Kindler, P., Guillevic, M., Baumgartner, M., Schwander, J., Landais, A., and Leuenberger, M.: Temperature reconstruction from 10 to 120 kyr b2k from the NGRIP ice core, Climate of the Past, 10, 887–902, 2014.

Kulp, S. A. and Strauss, B. H.: New elevation data triple estimates of global vulnerability to sea-level rise and coastal flooding, Nature Communications, 10, 4844, https://doi.org/10.1038/s41467-019-12808-z, 2019.

https://doi.org/10.5194/egusphere-2026-3331
Preprint. Discussion started: 25 June 2026

Larsen, N. K., Søndergaard, A. S., Levy, L. B., Olsen, J., Strunk, A., Bjørk, A. A., and Skov, D. S.: Contrasting modes of deglaciation between fjords and inter-fjord areas in eastern North Greenland, Boreas, 49, 903–917, https://doi.org/10.1111/bor.12455, 2020.

Larsen, N. K., Søndergaard, A. S., Levy, L. B., Strunk, A., Skov, D. S., Bjørk, A., Khan, S. A., and Olsen, J.: Late glacial and Holocene glaciation history of North and Northeast Greenland, Arctic, Antarctic, and Alpine Research, 54, 294–313, https://doi.org/10.1080/15230430.2022.2096773, 2022.

Lauritzen, M. L., Solgaard, A. M., Rathmann, N. M., Vinther, B. M., Grindsted, A., Noël, B., Aðalgeirsdóttir, G., and Hvidberg, C. S.: Modeled Greenland Ice Sheet evolution constrained by ice-core-derived Holocene elevation histories, EGUsphere, 2024, 1–29, 2024.

Le Meur, E. and Huybrechts, P.: A comparison of different ways of dealing with isostasy: examples from modelling the Antarctic ice sheet during the last glacial cycle, Annals of Glaciology, 23, 309–317, https://doi.org/10.3189/S0260305500013586, 1996.

Lecavalier, B. S., Milne, G. A., Vinther, B. M., Fisher, D. A., Dyke, A. S., and Simpson, M. J.: Revised estimates of Greenland ice sheet thinning histories based on ice-core records, Quaternary Science Reviews, 63, 73–82, https://doi.org/https://doi.org/10.1016/j.quascirev.2012.11.030, 2013.

Lecavalier, B. S., Milne, G. A., Simpson, M. J. R., Wake, L., Huybrechts, P., Tarasov, L., Kjeldsen, K. K., Funder, S., Long, A. J., Woodroffe, S., Dyke, A. S., and Larsen, N. K.: A model of Greenland ice sheet deglaciation constrained by observations of relative sea level and ice extent, Quaternary Science Reviews, 102, 54–84, https://doi.org/10.1016/j.quascirev.2014.07.018, 2014.

Lecavalier, B. S., Fisher, D. A., Milne, G. A., Vinther, B. M., Tarasov, L., Huybrechts, P., Lacelle, D., Main, B., Zheng, J., Bourgeois, J., and Dyke, A. S.: High Arctic Holocene temperature record from the Agassiz ice cap and Greenland ice sheet evolution, Proceedings of the National Academy of Sciences, 114, 5952–5957, https://doi.org/10.1073/pnas.1616287114, 2017.

Leger, T. P. M., Clark, C. D., Huynh, C., Jones, S., Ely, J. C., Bradley, S. L., Diemont, C., and Hughes, A. L. C.: A Greenland-wide empirical reconstruction of paleo ice sheet retreat informed by ice extent markers: PaleoGrIS version 1.0, Climate of the Past, 20, 701–755, https://doi.org/10.5194/cp-20-2024, 2024.

Leger, T. P. M., Ely, J. C., Clark, C. D., Bradley, S. L., Archer, R. E., and Zhu, J.: The Greenland-Ice-Sheet evolution over the last 24 000 years: insights from model simulations evaluated against ice-extent markers, The Cryosphere, 19, 5719–5761, https://doi.org/10.5194/tc-19-5719-2025, 2025.

Lesnek, A. J., Briner, J. P., Young, N. E., and Cuzzone, J. K.: Maximum southwest Greenland ice sheet recession in the early Holocene, Geophysical Research Letters, 47, e2019GL083 164, https://doi.org/10.1029/2019GL083164, 2020.

Lipscomb, W. H., Price, S. F., Hoffman, M. J., Leguy, G. R., Bennett, A. R., Bradley, S. L., Evans, K. J., Fyke, J. G., Kennedy, J. H., Perego, M., Ranken, D. M., Sacks, W. J., Salinger, A. G., Vargo, L. J., and Worley, P. H.: Description and evaluation of the Community Ice Sheet Model (CISM) v2.1, Geoscientific Model Development, 12, 387–424, https://doi.org/10.5194/gmd-12-387-2019, 2019.

Liu, Z., Otto-Bliesner, B. L., He, F., Brady, E. C., Tomas, R., Clark, P. U., Carlson, A. E., Lynch-Stieglitz, J., Curry, W., Brook, E., Erickson, D., Jacob, R., Kutzbach, J., and Cheng, J.: Transient Simulation of Last Deglaciation with a New Mechanism for Bølling-Allerød Warming, Science, 325, 310–314, https://doi.org/10.1126/science.1171041, 2009.

Liu, Z., Richardson, D., Lynch-Stieglitz, J., Otto-Bliesner, B. L., Clark, P. U., Marcott, S. A., Russell, J. M., Galy, A., Asmerom, Y., Jenson, J. W., and Goodman, R. E.: Evolution of the Atlantic meridional overturning circulation during the last deglaciation, Proceedings of the National Academy of Sciences, 109, 17 332–17 335, https://doi.org/10.1073/pnas.1207851109, 2012.

Lundberg, S. M., Erion, G., Chen, H., DeGrave, A., Prutkin, J. M., Nair, B., Katz, R., Himmelfarb, J., Bansal, N., and Lee, S.-I.: From local explanations to global understanding with explainable AI for trees, Nature Machine Intelligence, 2, 56–67, https://doi.org/10.1038/s42256-019-0138-9, 2020.

https://doi.org/10.5194/egusphere-2026-3331
Preprint. Discussion started: 25 June 2026

Milne, G. A., Latychev, K., Schaeffer, A., Crowley, J. W., Lecavalier, B. S., and Audette, A.: The influence of lateral Earth structure on glacial isostatic adjustment in Greenland, Geophysical Journal International, 214, 1252–1266, https://doi.org/10.1093/gji/ggy189, 2018.

Morlighem, M., Williams, C. N., Rignot, E., An, L., Arndt, J. E., Bamber, J. L., Catania, G., Chauché, N., Dowdeswell, J. A., Dorschel, B., et al.: BedMachine v3: Complete bed topography and ocean bathymetry mapping of Greenland from multibeam echo sounding combined with mass conservation, Geophysical research letters, 44, 11–051, 2017.

Mouginot, J., Rignot, E., Bjørk, A. A., van den Broeke, M., Millan, R., Morlighem, M., Noël, B., Scheuchl, B., and Wood, M.: Forty-six years of Greenland Ice Sheet mass balance from 1972 to 2018, Proceedings of the National Academy of Sciences, 116, 9239–9244, https://doi.org/10.1073/pnas.1904242116, 2019.

Nielsen, L. T., Aðalgeirsdóttir, G., Gkinis, V., Nuterman, R., and Hvidberg, C. S.: The effect of a Holocene climatic optimum on the evolution of the Greenland ice sheet during the last 10 kyr, Journal of Glaciology, 64, 477–488, https://doi.org/10.1017/jog.2018.39, 2018.

Pollard, D., Chang, W., Haran, M., Applegate, P., and DeConto, R.: Large ensemble modeling of the last deglacial retreat of the West Antarctic Ice Sheet: comparison of simple and advanced statistical techniques, Geoscientific Model Development, 9, 1697–1723, https://doi.org/10.5194/gmd-9-1697-2016, 2016.

Quiquet, A., Roche, D. M., Dumas, C., Bouttes, N., and Lhardy, F.: Climate and ice sheet evolutions from the last glacial maximum to the pre-industrial period with an ice-sheet–climate coupled model, Climate of the Past, 17, 2179–2199, https://doi.org/10.5194/cp-17-2179-2021, 2021.

Robinson, A. and Goelzer, H.: The importance of insolation changes for paleo ice sheet modeling, The Cryosphere, 8, 1419–1428, https://doi.org/10.5194/tc-8-1419-2014, 2014.

Robinson, A., Calov, R., and Ganopolski, A.: Multistability and critical thresholds of the Greenland ice sheet, Nature Climate Change, 2, 429–432, 2012.

Robinson, A., Alvarez-Solas, J., Montoya, M., Goelzer, H., Greve, R., and Ritz, C.: Description and validation of the ice-sheet model Yelmo (version 1.0), Geoscientific Model Development, 13, 2805–2823, https://doi.org/10.5194/gmd-13-2805-2020, 2020.

Robinson, A., Goldberg, D., and Lipscomb, W. H.: A comparison of the stability and performance of depth-integrated ice-dynamics solvers, The Cryosphere, 16, 689–709, https://doi.org/10.5194/tc-16-689-2022, 2022.

Sbarra, C. M., Briner, J. P., Graham, B. L., Poinar, K., Thomas, E. K., and Young, N. E.: Evidence for a more extensive Greenland Ice Sheet in southwestern Greenland during the Last Glacial Maximum, Geosphere, 18, 1493–1506, https://doi.org/10.1130/GES02432.1, 2022.

Shapley, L. S.: A Value for n-Person Games, in: Contributions to the Theory of Games II, edited by Kuhn, H. W. and Tucker, A. W., no. 28 in Annals of Mathematics Studies, pp. 307–317, Princeton University Press, Princeton, https://doi.org/10.1515/9781400881970-018, 1953.

Simpson, M. J., Milne, G. A., Huybrechts, P., and Long, A. J.: Calibrating a glaciological model of the Greenland ice sheet from the Last Glacial Maximum to present-day using field observations of relative sea level and ice extent, Quaternary Science Reviews, 28, 1631–1657, https://doi.org/https://doi.org/10.1016/j.quascirev.2009.03.004, quaternary Ice Sheet-Ocean Interactions and Landscape Responses, 2009.

Steffen, R., Audet, P., and Lund, B.: Weakened lithosphere beneath Greenland inferred from effective elastic thickness: A hot spot effect?, Geophysical Research Letters, 45, 4733–4742, https://doi.org/10.1029/2017GL076885, 2018.

Stein, M.: Large Sample Properties of Simulations Using Latin Hypercube Sampling, Technometrics, 29, 143–151, https://doi.org/10.1080/00401706.1987.10488205, 1987.

Stone, E., Lunt, D., Rutt, I., and Hanna, E.: Investigating the sensitivity of numerical model simulations of the modern state of the Greenland ice-sheet and its future response to climate change, The Cryosphere, 4, 397–417, 2010.

https://doi.org/10.5194/egusphere-2026-3331
Preprint. Discussion started: 25 June 2026

Tabone, I., Blasco, J., Robinson, A., Alvarez-Solas, J., and Montoya, M.: The sensitivity of the Greenland Ice Sheet to glacial–interglacial oceanic forcing, Climate of the Past, 14, 455–472, https://doi.org/10.5194/cp-14-455-2018, 2018.

Tabone, I., Robinson, A., Montoya, M., and Alvarez-Solas, J.: Holocene thinning in central Greenland controlled by the Northeast Greenland Ice Stream, Nature communications, 15, 6434, 2024.

Tarasov, L. and Peltier, W. R.: Greenland glacial history and local geodynamic consequences, Geophysical Journal International, 150, 198–229, https://doi.org/10.1046/j.1365-246X.2002.01702.x, 2002.

Thomas, E. K., Briner, J. P., Ryan-Henry, J., and Huang, Y.: A major increase in winter snowfall during the middle Holocene on western Greenland caused by reduced sea ice in Baffin Bay and the Labrador Sea, Geophysical Research Letters, 43, 5302–5311, https://doi.org/10.1002/2016GL068513, 2016.

Vasskog, K., Langebroek, P. M., Andrews, J. T., Nilsen, J. E. Ø., and Nesje, A.: The Greenland Ice Sheet during the last glacial cycle: Current ice loss and contribution to sea-level rise from a palaeoclimatic perspective, Earth-Science Reviews, 150, 45–67, 2015.

Vinther, B. M., Buchardt, S. L., Clausen, H. B., Dahl-Jensen, D., Johnsen, S. J., Fisher, D., Koerner, R., Raynaud, D., Lipenkov, V., Andersen, K. K., et al.: Holocene thinning of the Greenland ice sheet, Nature, 461, 385–388, 2009.

Waelbroeck, C., Labeyrie, L., Michel, E., Duplessy, J. C., McManus, J. F., Lambeck, K., Balbon, E., and Labracherie, M.: Sea-level and deep water temperature changes derived from benthic foraminifera isotopic records, Quaternary Science Reviews, 21, 295–305, https://doi.org/10.1016/S0277-3791(01)00101-9, ePILOG, 2002.

Whitehouse, P. L., Bentley, M. J., and Le Brocq, A. M.: A deglacial model for Antarctica: geological constraints and glaciological modelling as a basis for a new model of Antarctic glacial isostatic adjustment, Quaternary Science Reviews, 32, 1–24, https://doi.org/https://doi.org/10.1016/j.quascirev.2011.11.016, 2012.

Willemse, N. W., Koster, E. A., Hoogakker, B., and van Tatenhove, F. G. M.: A continuous record of Holocene eolian activity in West Greenland, Quaternary Research, 59, 322–334, https://doi.org/10.1016/S0033-5894(03)00037-1, 2003.

Wilson, N., Straneo, F., and Heimbach, P.: Satellite-derived submarine melt rates and mass balance (2011–2015) for Greenland's largest remaining ice tongues, The Cryosphere, 11, 2773–2782, https://doi.org/10.5194/tc-11-2773-2017, 2017.

Yang, H., Krebs-Kanzow, U., Kleiner, T., Sidorenko, D., Rodehacke, C. B., Shi, X., Gierz, P., Niu, L., and Lohmann, G.: Impact of paleoclimate on present and future evolution of the Greenland Ice Sheet, PLOS ONE, 17, e0259 816, https://doi.org/10.1371/journal.pone.0259816, 2022.

Young, N. E. and Briner, J. P.: Holocene evolution of the western Greenland Ice Sheet: Assessing geophysical ice-sheet models with geological reconstructions of ice-margin change, Quaternary Science Reviews, 114, 1–17, https://doi.org/https://doi.org/10.1016/j.quascirev.2015.01.018, 2015.

Young, N. E., Lesnek, A. J., Cuzzone, J. K., Briner, J. P., Badgeley, J. A., Balter-Kennedy, A., Graham, B. L., Cluett, A., Lamp, J. L., Schwartz, R., Tuna, T., Bard, E., Caffee, M. W., Zimmerman, S. R. H., and Schaefer, J. M.: In situ cosmogenic ^{10}Be–^{14}C–^{26}Al measurements from recently deglaciated bedrock as a new tool to decipher changes in Greenland Ice Sheet size, Climate of the Past, 17, 419–450, https://doi.org/10.5194/cp-17-419-2021, 2021.